nature neuroscience

Article

https://doi.org/10.1038/s41593-024-01849-3

NOMPC ion channel hinge forms a gating spring that initiates mechanosensation

Received: 26 September 2023

Accepted: 12 November 2024

Published online: 6 January 2025

Check for updates

Philip Hehlert[1,7], Thomas Effertz[2,7], Ruo-Xu Gu[3,5], Björn Nadrowski[1], Bart R. H. Geurten[1,6], Dirk Beutner[2], Bert L. de Groot[3,4] & Martin C. Göpfert[1,4]

The sensation of mechanical stimuli is initiated by elastic gating springs that pull open mechanosensory transduction channels. Searches for gating springs have focused on force-conveying protein tethers such as the amino-terminal ankyrin tether of the *Drosophila* mechanosensory transduction channel NOMPC. Here, by combining protein domain duplications with mechanical measurements, electrophysiology, molecular dynamics simulations and modeling, we identify the NOMPC gating-spring as the short linker between the ankyrin tether and the channel gate. This linker acts as a Hookean hinge that is ten times more elastic than the tether, with the linker hinge dictating channel gating and the intrinsic stiffness of the gating spring. Our study shows how mechanosensation is initiated molecularly; disentangles gating springs and tethers, and respective paradigms of channel gating; and puts forward gating springs as core ion channel constituents that enable efficient gating by diverse stimuli and in a wide variety of channels.

Our abilities to sense touch, gravity and sound—and to control movements of our gut and limbs—all commence with the transduction of mechanical stimuli into electrical signals[1–4]. This mechano-electrical transduction (MET) takes place in mechanosensory cells and is mediated by MET channels—dedicated ion channels that are gated directly by mechanical stimuli[5–8]. When this mechano-gating of MET channels was uncovered four decades ago, in mechanosensory hair cells of the inner ear[9–12], it was realized that coupling mechanical stimuli to channel gating transitions necessitates an elastic coupling element[10]—the gating spring[11]—whose force-induced deformation delivers the gating energy[10–12]. Through its elasticity, this gating spring allows the channel to switch between closed and open conformations, and mechanical stimuli can influence the channel open probability by altering the tension of the gating spring[1,10–14].

Irrespective of whether a gating spring opens a MET channel by push or pull, the spring will relax when the channel gates swings open, making it seem more compliant[1,12–14]. This gating compliance is an intrinsic property of MET channels[1] that has been observed experimentally in the mechanics of both vertebrate inner ear hair cells[12,15–17] and the *Drosophila* ear[18]. In either system, the stiffness of the gating springs can be deduced using the gating-spring model[1,12–18]—a biophysical framework that, linking gating compliance to MET channel gating, defines the gating spring as a theoretical element[1,12–14].

MET channels can receive force from the surrounding lipid bilayer (force-from-lipids gating) and tether filaments (force-from-filaments gating)[2–8]. Searches for gating springs have concentrated on tether filaments that, judging from their position and stiffness, could potentially serve as gating springs. In vertebrate hair cells, the gating springs might be the tip links that, tethering the MET channel complex extracellularly to adjacent hair bundle stereocilia, convey force to the channels[11–14,17,19–21]. The whole tip links, however, might not be sufficiently compliant to function as gating springs[22–26]. Alternative gating-spring candidates are the tip link component protocadherin-15 (refs. 27,28) and ankyrin repeat (AR) proteins that tether membrane

[1]Department of Cellular Neurobiology, University of Göttingen, Göttingen, Germany. [2]Department of Otorhinolaryngology, Head and Neck Surgery and InnerEarLab, University Medical Center Göttingen, Göttingen, Germany. [3]Computational Biomolecular Dynamics Group, Max Planck Institute for Multidisciplinary Sciences, Göttingen, Germany. [4]Multiscale Bioimaging Cluster of Excellence (MBExC), University of Göttingen, Göttingen, Germany. [5]Present address: School of Life Sciences and Biotechnology, Shanghai Jiao Tong University, Shanghai, China. [6]Present address: Department of Zoology, University of Otago, Dunedin, New Zealand. [7]These authors contributed equally: Philip Hehlert, Thomas Effertz. e-mail: mgoepfe@gwdg.de

https://doi.org/10.1038/s41593-024-01849-3

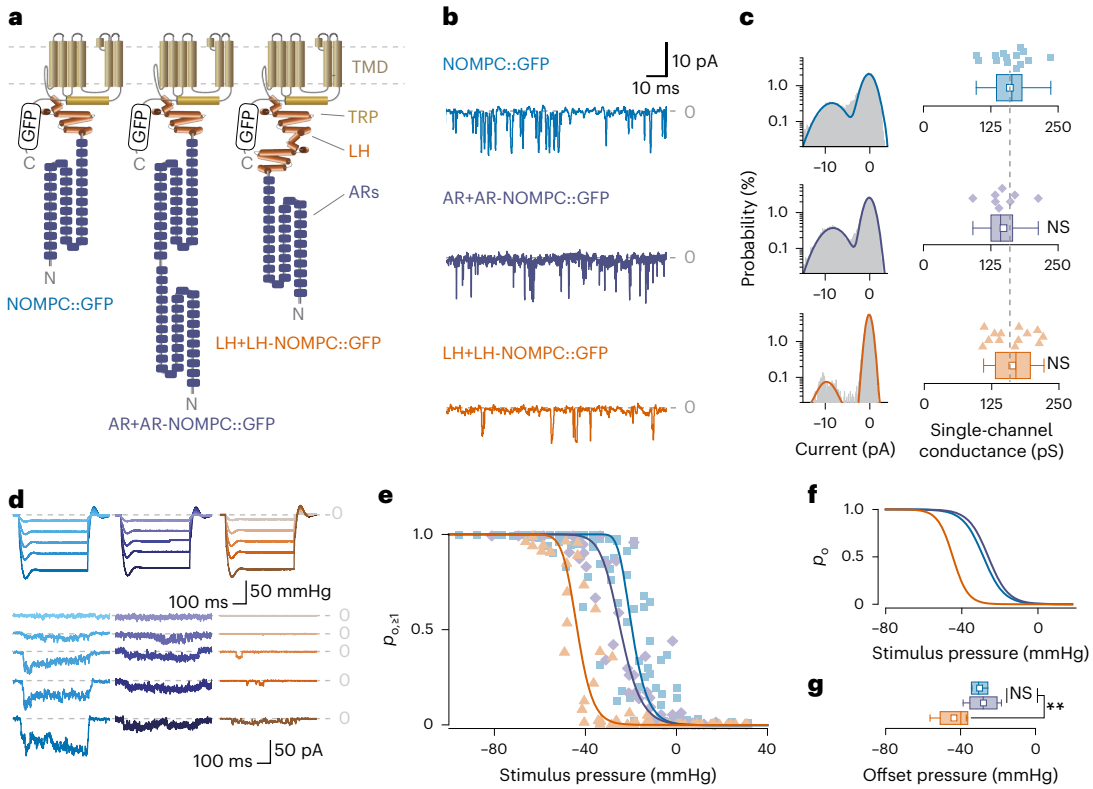

Fig. 1 | Effects of domain duplications on in vitro NOMPC function. **a**, Sketches of NOMPC::GFP control protein, AR+AR–NOMPC::GFP with duplicated AR domain, and LH+LH–NOMPC::GFP with duplicated LH domain. TMD, transmembrane domain (membrane core). **b**, Representative traces of respective spontaneous currents recorded in outside–out patches at a holding potential of −60 mV. Dashed lines, zero current level (0 V); $n = 22$ (NOMPC::GFP), 7 (AR+AR–NOMPC::GFP) or 13 (LH+LH–NOMPC::GFP) cells. **c**, Respective histograms of current amplitudes, each fitted with two Gaussians (left), and single-channel conductance. Right, boxplot of data (gray dotted line, average from control; box, 50% of data; line in box, median; white square, mean, whiskers, 1.5× interquartile range). **d**, Representative recordings of respective pressure-activated currents; $n = 8$ (NOMPC::GFP), 6 (AR+AR–NOMPC::GFP) or 7 (LH+LH–NOMPC::GFP) cells. **e**, Respective probability to find at least one channel constantly open, $p_{o,\geq 1}$, plotted against the stimulus pressure (symbols), fitted with $Y(X) = 1 - (1 - p_o(X))^N$ (lines); color code as in **a**–**d**. **f**, Respective open probability, p_o, (top) deduced from the fits in **e**. **g**, Respective offset pressures corresponding to $p_o = 0.5$. Boxplot as defined in **c**. Two-tailed Mann–Whitney *U*-tests with Bonferroni correction (NS, not significant; $^*P < 0.05$; $^{**}P < 0.01$; $^{***}P < 0.001$). For additional data, see Extended Data Fig. 1b,c.

proteins intracellularly to the cytoskeleton[19,20,23,25,29]. In the nematode *Caenorhabditis elegans*, the AR protein ankyrin seems to convey force to a MET channel complex that, molecularly, resembles that of hair cells[29], and ARs are thought to form the gating spring of the *Drosophila* MET channel NOMPC[30–39]. NOMPC is a mechano-gated transient receptor potential (TRP) family channel implicated in touch sensation[32,40], proprioception[41] and hearing[42]. Compared with other TRP channels, NOMPC bears an exceptionally long N-terminal AR domain that forms one full turn of a helix[30,35]. Tethering the channel to microtubules[33–35], this AR domain forms a force-conveying filament[33,34,37] that is essential for mechano-gating[34]. Apart from tether filaments, the lipid bilayer has been put forward as a gating-spring candidate[43] and, in principle, any compliant force-conveying element, or several such elements together, could function as gating spring[25,26].

For a coupling element to qualify as a gating-spring component, manipulating its stiffness should alter the gating-spring stiffness and, thus, channel gating[19,20]. Softening the element should necessitate larger displacements to force open the channel, and it should also reduce the propensity of the channel to open spontaneously by reducing the resting tension of the spring[19–21,34,37]. Such stiffness manipulations, though proposed[19,20], are unreported, leaving unresolved the molecular identities of the gating springs[17,19,20,23–26,38].

The stiffness of a Hookean spring scales inversely with length, and stacks of ARs reportedly display Hookean behavior, with their stiffness declining when more ARs are added to the stacks[23,44]. A total of 29 ARs form the AR domain of the NOMPC channel[40], whereby duplicating this domain yields functional 29+29ARs–NOMPC channels whose AR domain comprises twice 29 ARs[34]. Judging from electron tomography, the AR domain of 29+29ARs–NOMPC has twice the normal length[37], suggesting that its stiffness will be halved. We now tested how this domain duplication affects NOMPC gating and the gating-spring stiffness, unexpectedly revealing that the NOMPC gating spring is not its AR domain but, instead, its linker helix (LH) domain, which is interspersed between AR domain and gate.

Results

AR domain duplication leaves NOMPC gating unaltered in vitro

To explore how AR domain duplication affects NOMPC gating, we expressed 29AR+29AR-NOMPC[34] (hereafter referred to as AR+AR–NOMPC::GFP; Fig. 1a) heterologously in *Drosophila* S2 cells, transfecting cells with the parental *nompC-GFP* plasmid as controls. The latter plasmid includes the 1,732-amino-acid isoform *nompC.L* (GenBank: ADK73985.1), tagged with green fluorescent protein (GFP)[37] (hereafter referred to as NOMPC::GFP; Fig. 1a). GFP fluorescence documented cell surface localization for both the control protein, NOMPC::GFP and the modified protein AR+AR-NOMPC::GFP (Extended Data Fig. 1a). In accordance with previous observations[34], patch-clamp recordings from excised outside–out membrane patches confirmed that both proteins form functional ion channels displaying spontaneous openings (Fig. 1b). Current amplitude histograms obtained for the two

https://doi.org/10.1038/s41593-024-01849-3

proteins showed similar bimodal distributions (Fig. 1c, left), whereby fitting each distribution with two Gaussians yielded a virtually identical single-channel conductance for AR+AR–NOMPC::GFP and NOMPC::GFP (Fig. 1c, right). Both proteins gave rise to mechano-activated currents when we applied negative pressure to the inside of the patch using a high-speed pressure clamp[45] (Fig. 1d). Increasing the pressure amplitude opened several channels and extended their open times (Fig. 1d) and, accordingly, we determined the probability of finding at least one channel open, $p_{o,\geq 1} = 1 - (1 - p_o)^N$, where p_o and N are the open probability and the channel number, respectively. When plotted against the pressure amplitude, P, $p_{o,\geq 1}(P)$ was shifted to slightly more negative pressures for AR+AR–NOMPC::GFP than for NOMPC::GFP (Fig. 1e). Fitting $p_{o,\geq 1}(P)$ with $Y(P) = 1 - (1 - p_o(P))^N$ attributed this shift to a lower number, N, of active AR+AR–NOMPC::GFP channels in the membrane patches (1.7 ± 0.3 channels per patch versus 9 ± 1.8 channels per patch for NOMPC::GFP; mean ± s.e.m.; sample sizes, seven and eight cells, respectively) (Extended Data Fig. 1b). The deduced open probabilities, $p_o(P)$, superimposed for the two proteins (Fig. 1f), with the pressure amplitude corresponding to $p_o = 0.5$ being virtually identical for NOMPC::GFP and AR+AR–NOMPC::GFP (Fig. 1g and Extended Data Fig. 1c). Hence, under in vitro conditions, duplication of the NOMPC AR domain seems to have, at most, subtle effects on NOMPC spontaneous activity and mechanosensitivity.

AR domain duplication does not alter NOMPC function in vivo

NOMPC is expressed widely in *Drosophila* mechanosensory cells, including the ciliated chordotonal stretch receptor neurons of Johnston's organ (JO)—the fly's antennal hearing organ[40,46]. Within JO neurons, NOMPC localizes to mechanosensory cilium tips[46], with its loss causing an approximately threefold drop in JO mechanosensitivity[42]. To explore whether AR domain duplication might affect NOMPC function in vivo, we introduced AR+AR–NOMPC::GFP and NOMPC::GFP in the JO neurons of *nompC* null mutant ($nompC^{-/-}$) flies using the UAS/Gal4 system[47] with *nompC-Gal4* (ref. 41). GFP fluorescence confirmed that, within JO neurons, both proteins localize to the cilium tips (Extended Data Fig. 2). To probe mechanosensitivity, we recorded JO neuron compound action potentials (CAPs) while displacing the fly's antennal sound receiver with force steps (Fig. 2). Compared with NOMPC::GFP controls (Fig. 2a), receiver displacements that were 3.4 times greater were required to evoke the half-maximum CAP response in $nompC^{-/-}$ null mutant flies (Fig. 2b,e), reporting the roughly threefold sensitivity drop. Normal sensitivity, as seen in the wild type[42], was restored equally by NOMPC::GFP and AR+AR–NOMPC::GFP (Fig. 2a,c,e), documenting that either protein can compensate for the loss of endogenous NOMPC. Hence, in the JO neurons of live flies, AR+AR–NOMPC::GFP, NOMPC::GFP and endogenous NOMPC are interchangeable functionally, illustrating that, also under in vivo conditions, duplication of the AR domain does not notably compromise the mechanosensory function of NOMPC.

AR domain duplication does not affect gating-spring stiffness

To test whether AR domain duplication might alter gating-spring stiffness, we measured the gating compliance in the mechanics of the fly's antennal sound receiver[18]. Displacements of this receiver are coupled to JO neuron cilia, and the receiver stiffness drops nonlinearly over that range of displacement amplitudes in which MET channels gate[18,31,48]. Quantitatively, this gating compliance can be described by a gating-spring model including opposing populations of two channel types that differ in displacement sensitivity[31]. We showed previously that the gating compliance contributed by the more sensitive channel type is lost selectively in $nompC^{-/-}$ flies[31], and we now found that this NOMPC-dependent gating compliance is restored fully by both NOMPC::GFP and AR+AR–NOMPC::GFP. Replacing native NOMPC with either protein rescued the sharp drop of the receiver stiffness at small displacement amplitudes (Fig. 3a,c) that is seen in wild-type flies[31] and lost in $nompC^{-/-}$ flies (Fig. 3b).

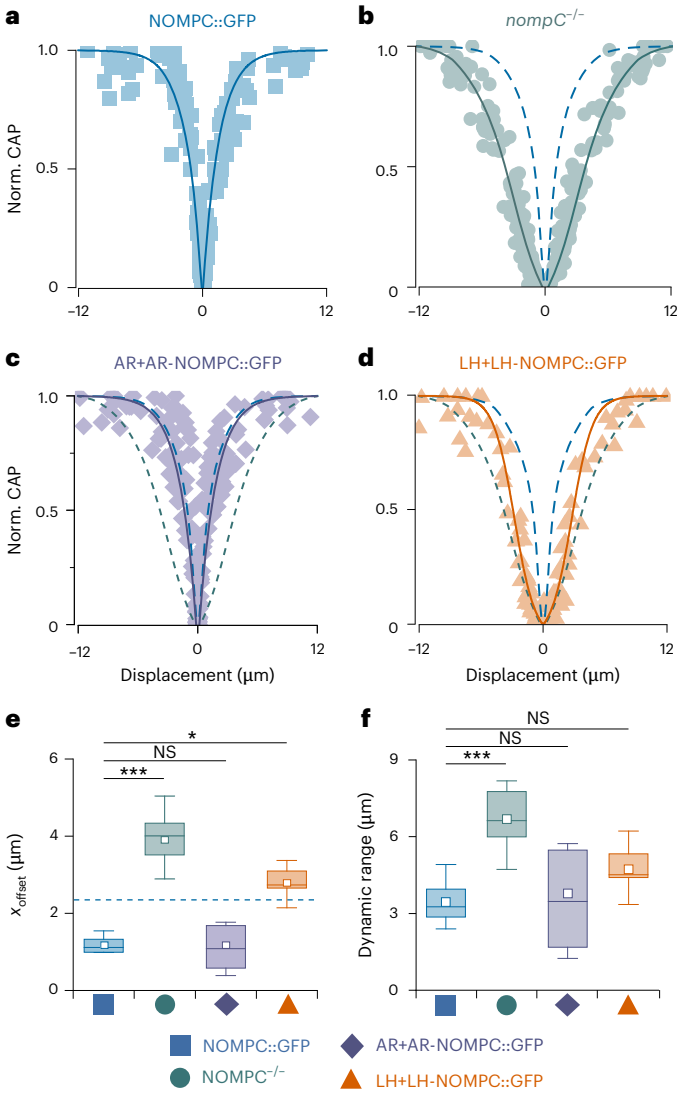

Fig. 2 | Effects of domain duplications on JO neuron CAP responses. **a**–**d**, Normalized (norm.) CAP amplitude plotted against sound receiver displacement (symbols) ($n \geq 5$ flies per strain) and average Boltzmann fits (lines) for NOMPC::GFP (*nompC*^{3}, *Gal4 > UAS-nompC.L-GFP* flies) (**a**), $nompC^{-/-}$ (*nompC*^{3} null mutants; dashed blue line, respective fit from **a**) (**b**), AR+AR–NOMPC::GFP (*nompC*^{1}, *nompC-Gal4 > UAS-AR+AR-nompC.L-GFP* flies; dashed blue line, fit from **a**; short-dashed dark-teal line, fit from **b**) (**c**), and LH+LH–NOMPC::GFP (*nompC*^{3}, *nompC-Gal4 > UAS-LH+LH-nompC.L-GFP* flies, lines as in **c**) (**d**). **e**, Boxplots showing respective displacement corresponding to the half-maximum CAP amplitude (box, 50% of data; line in box, median; white square, mean; whiskers, 1.5× interquartile range). Compared with NOMPC::GFP and AR+AR–NOMPC::GFP flies, this displacement is increased around twofold (dashed line) in flies expressing LH+LH–NOMPC::GFP. Two-tailed Mann–Whitney *U*-tests with Bonferroni correction. **f**, Respective dynamic range of the CAP response, measured as the displacement range corresponding to 10–90% of maximum CAP amplitude. Statistics and boxplot as in **e**.

To describe this sharp stiffness drop, the gating-spring model had to include two channel types, the same as for wild-type flies[31], as confirmed by assessing the goodness of the fits using Akaike weights (Supplementary Table 1). Across displacement amplitudes, the receiver stiffness superimposed for flies expressing either protein, as did respective fits of the gating-spring model (Fig. 3a,c). Judging from these fits, opening one of the NOMPC-dependent sensitive (s) channels changes the force in its gating spring, $z_s = \gamma\kappa_s\delta_s$ (refs. 1,12–14), by 24 ± 1 fN (mean ± s.e.m.) in flies expressing AR+AR–NOMPC::GFP (Fig. 3e and Supplementary Table 1). This force change matches that reported for wild-type flies

https://doi.org/10.1038/s41593-024-01849-3

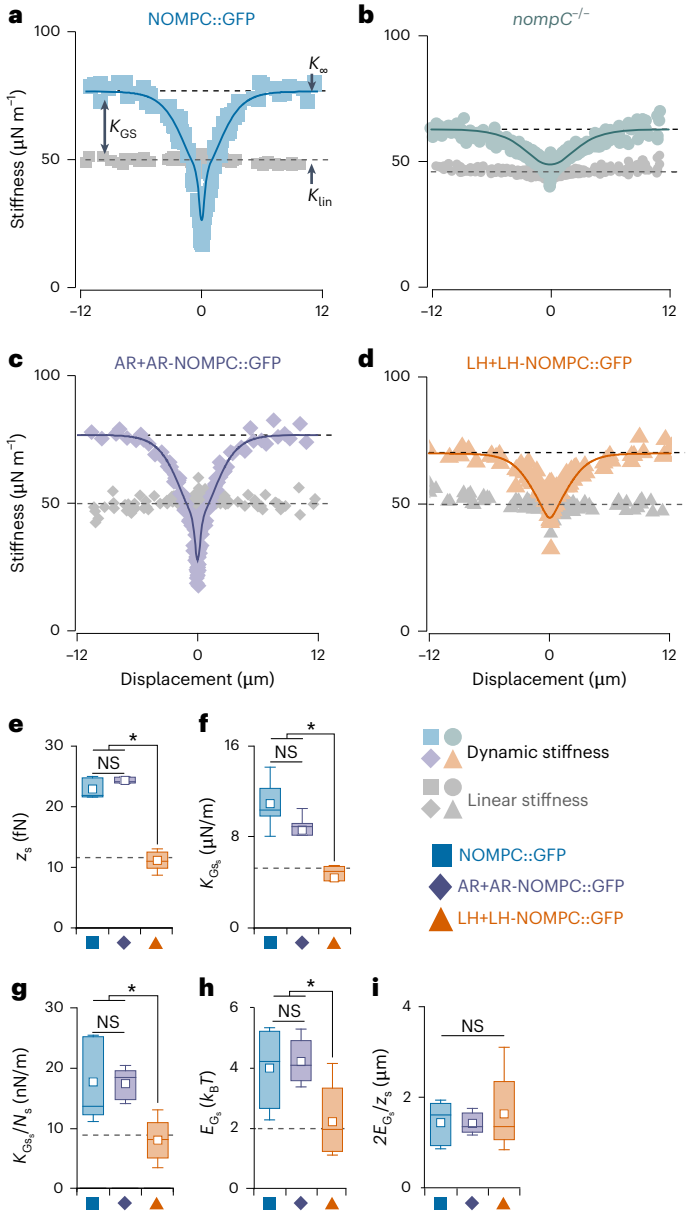

Fig. 3 | Effects of domain duplications on gating compliance and gating-spring stiffness. a–**d**, Dynamic (colored symbols) and linear stiffness (K_{lin}, gray symbols) of the fly's antennal sound receiver plotted against receiver displacement. Solid lines, fitted gating-spring model; dashed lines, mean linear (K_{lin}) and asymptotic (K_∞) stiffness for NOMPC::GFP (*nompC*^{3}, *nompC-Gal4 > UAS-nompC.L-GFP* flies) (**a**), *nompC*$^{-/-}$ (*nompC*^{3} null mutants) (**b**), AR+AR–NOMPC::GFP (*nompC*^{1}, *nompC-Gal4 > UAS-AR+AR-nompC.L-GFP* flies) (**c**) and LH+LH–NOMPC::GFP (*nompC*^{3}, *nompC-Gal4 > UAS-LH+LH-nompC.L-GFP* flies) (**d**). $n = 5$ flies per strain except $n = 19$ (*nompC*$^{-/-}$). **e**–**i**, Boxplots of parameter values deduced from the fits in **a**–**d** (box, 50% of data around median; line in box, median; white square, mean; whiskers, 1.5× interquartile range). Two-tailed Mann–Whitney *U*-tests with Bonferroni correction. Dashed lines, twofold reduction compared with NOMPC::GFP controls. **e**, Change in force, z_s, in a NOMPC-dependent gating spring upon channel opening. **f**, Combined effective stiffness, K_{GS_s}, of NOMPC-dependent gating springs. **g**, K_{GS_s} normalized to N_s, the number of NOMPC-dependent channels. **h**, Energy required to open a single NOMPC-dependent channel, E_{G_s}, in multiples of thermal energy, k_BT (4.1 zJ). **i**, Projected gating swing, $\delta_s/\gamma = 2E_{G_s}/z_s$. For parameter values, see Supplementary Table 1.

(24 ± 1 fN)[31] and that obtained for flies expressing NOMPC::GFP (23 ± 2 fN; Fig. 3e and Supplementary Table 1). Duplicating the AR domain is unlikely to alter γ—a geometric projection factor relating receiver displacements to molecular displacements[12–14,18]—yet reductions of the gating-spring stiffness, κ_s, could, in principle, be balanced by an increased gating swing, δ_s. Evidence that the AR domain duplication does not alter κ_s—and thus δ_s—was provided by the asymptotic stiffness, K_∞, the antennal receiver approaches at large displacement amplitudes (Fig. 3a,c). According to the gating-spring model, $K_\infty = K_{lin} + K_{GS}$, where K_{lin} is the receiver's linear stiffness and K_{GS} is the combined stiffness contributed by all gating springs[1,12,31]. Parameter values obtained for K_∞, K_{lin} and K_{GS} were virtually identical for flies expressing AR+AR–NOMPC::GFP and NOMPC::GFP (Supplementary Table 1) and, judging from parameter values obtained for *nompC*$^{-/-}$ flies, the gating springs associated with the less sensitive (ls) channel type have a combined stiffness, $K_{GS_{ls}}$, of 17 ± 3 μN m^{-1} (mean ± s.e.m.), matching a previous estimate (16 ± 3 μN m^{-1})[31]. Using the former value to deduce the combined stiffness of the NOMPC-dependent gating springs, $K_{GS_s} = K_{GS} - K_{GS_{ls}} = N_s\gamma^2\kappa_s$, yielded slightly lower values of K_{GS_s} for flies expressing AR+AR–NOMPC::GFP than for NOMPC::GFP controls (Fig. 3f), reflecting a slightly, though statistically nonsignificant, lower channel number, N_s (Supplementary Table 1). When we normalized K_{GS_s} to N_s, the effective gating-spring stiffness per channel, $\gamma^2\kappa_s = K_{GS_s}/N_s$, was identical for AR+AR–NOMPC::GFP and NOMPC::GFP (Fig. 3g), signaling that the AR domain duplication does not alter the spring constant, k_s, of individual NOMPC-dependent gating springs. Also unaltered were the κ_s-dependent single-channel gating energy, $E_{G_s} = 1/2\kappa_s\delta_s^2 = 1/2\,(N_s z_s^2/K_{GS_s})$ [48] (Fig. 3h) and the κ_s-independent projected gating swing, $\delta_s/\gamma = 2E_{G_s}/z_s$ (Fig. 3i). Accordingly, the AR domain does not contribute detectably to gating-spring mechanics, indicating that this mechanics is determined by other, more compliant coupling elements.

Actuating ARs deforms LH domain hinge

The intracellular AR domain is connected to the NOMPC membrane core by the LH domain (Fig. 1a)—a stack of intracellular linker helices spanning approximately residues 1136–1260 of the NOMPC.L isoform (UniProt: A8DYV6_DROME)[35]. Judging from a high-resolution cryogenic electron microscopic structure of NOMPC.L (PDB 5VKQ) in the closed conformation[35] and respective molecular dynamics simulations[36,39], the LH domain seems to act as a bridge between the AR domain and the TRP domain, conveying force to the pore-forming transmembrane helices S5 and S6 (Fig. 1a and 4a). Domain swapping with voltage-gated channels had shown that, together, the NOMPC AR and LH domains mediate mechano-gating[34]. Accordingly, we reasoned that, instead of the AR domain, the LH domain could act as the gating spring. To assess whether the LH domain might be elastic and deform when force acts on the ARs, we performed molecular dynamics simulations for part of the reported NOMPC structure[35], including the last five ARs (AR25–AR29), the LH domain and the channel's membrane core (Fig. 4a). Besides applying pulling force to AR25, we also applied pushing force, which seems to activate NOMPC[39]. Both types of forcing induced larger conformational changes of the LH domain than the AR domains, as revealed by comparing the root-mean-square deviation (RMSD) of atomic positions between nonequilibrium (with force applied) and equilibrium (without force applied) simulations (Fig. 4b). Principal component analysis (PCA) revealed rigid body motion of the transmembrane helices relative to the ARs along the direction of the first principal component, which accounted for more than 50% of the total variance (Fig. 4c,d). Dynamic domain analysis of the extreme PCA conformations using the DynDom method[49] hinged this relative movement on residues of the LH domain (Fig. 4d and Supplementary Video 1). Aligning the transmembrane helices, the LH domain and the ARs of the extreme PCA conformations separately also located the main conformational differences at the LH and TRP domains, whereas the conformation of the AR domain remained almost unchanged (Fig. 4e). PCA of the LH domain alone revealed hinge-like motions of its upper half (amino acids 1218–1260) relative to its lower half (1235–1217) (Fig. 4f and Supplementary Videos 2–4). The collective motion of the LH domain alone correlated with that of the entire protein portion for their first principal component

https://doi.org/10.1038/s41593-024-01849-3

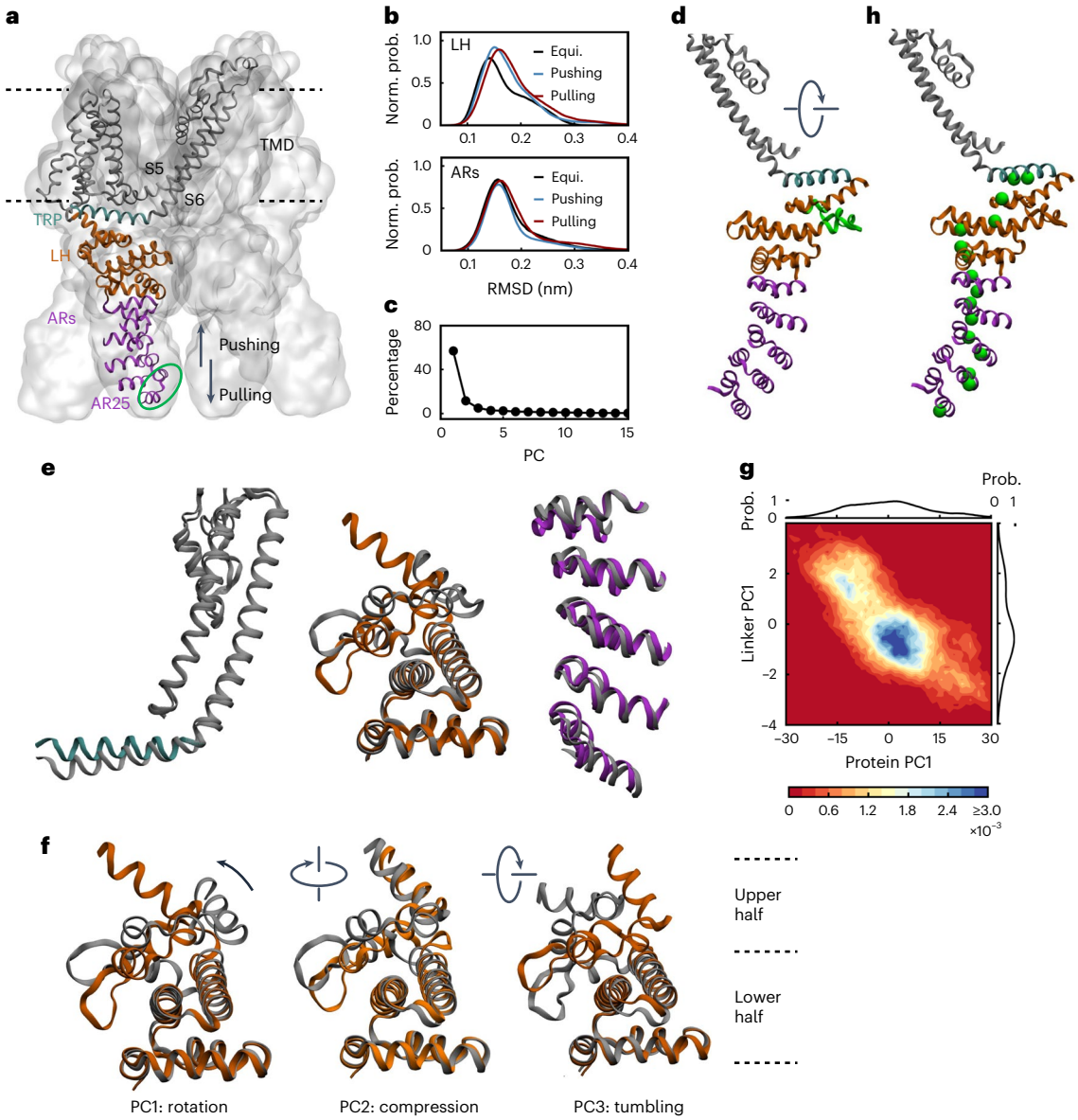

Fig. 4 | Pulling force acting on ARs deforms the LH domain. a, Structure of the truncated protein used in molecular dynamics simulations, depicting ARs and LH domains, TRP and TMD. **b**, Distributions of the RMSD of the LH and AR domains in simulations with and without force. For the AR domain, the RMSD was calculated for the α helix backbone. **c**, Relative contribution of principal components (PCs) to the total variance, in percentage. **d**, Rigid body movements of the core protein along the first PC, recognized by the DynDom method[49]. The identified rigid domains are in magenta (ARs), orange (LH) and gray (transmembrane helices), with hinge regions in green (Supplementary Video 1). **e**, Separate alignments of the pore helices (left), the LH domain (middle), and the ARs (right) for the extreme conformations along PC1 of the core protein. **f**, PCA on the LH domain alone. The extreme conformations along the first three PCs are aligned based on the lower half (residues 1135–1217) of the LH domain. Arrows, direction of movement (Supplementary Videos 2–4). **g**, Histogram of PC1 of the LH domain (linker PC1) as a function of the PC1 of the core protein (protein PC1). **h**, Residues occurring most in the identified communication pathways between the AR25 and the TRP helix; green balls, Cα atoms of these residues. For additional information, see Extended Data Fig. 3 and 4 and Supplementary Table 2. Equi., equilibrium; prob., probability.

(Pearson correlation coefficient of ~0.78; Fig. 4g). This motion coupling further corroborates the hinge function of the LH domain, with no other domains determining the collective motion of the simulated portion of the protein. To assess how the ARs communicate with the transmembrane domain, we searched for communication pathways between AR25 and the TRP domain using community network analysis[50]. All five ARs and the LH domain were found to be involved in the information flow, with the contacts between the LH and TRP domain mediating this flow between intracellular and transmembrane domains (Fig. 4h). In our simulations, the five ARs reflected the motion of the LH domain, hampering reasonable estimates of LH domain elasticity. The combined elasticity of the LH domain and the five ARs (Extended Data Fig. 3a), however, exceeded that obtained for those five ARs when force was applied to AR25 and the LH domain was restrained (Extended Data Fig. 3a,b), signaling that the LH domain is considerably more elastic than AR25–AR29. Compared with those 5 ARs, the 26 ARs spanning from AR4 to AR29 were much softer when force was applied to AR4 and the LH domain was restrained (Extended Data Fig. 3b), yet the conformational changes located mainly at the N-terminal ARs AR4–AR7, whose side chain structures are unresolved[35]. These localized conformational changes might not occur in nature, where the N-terminal end of the AR domain is bound to microtubules and other proteins seem to support the entire AR domain[37]. Hence, the LH domain hinge identified by our simulations could be sufficiently compliant to serve gating-spring

https://doi.org/10.1038/s41593-024-01849-3

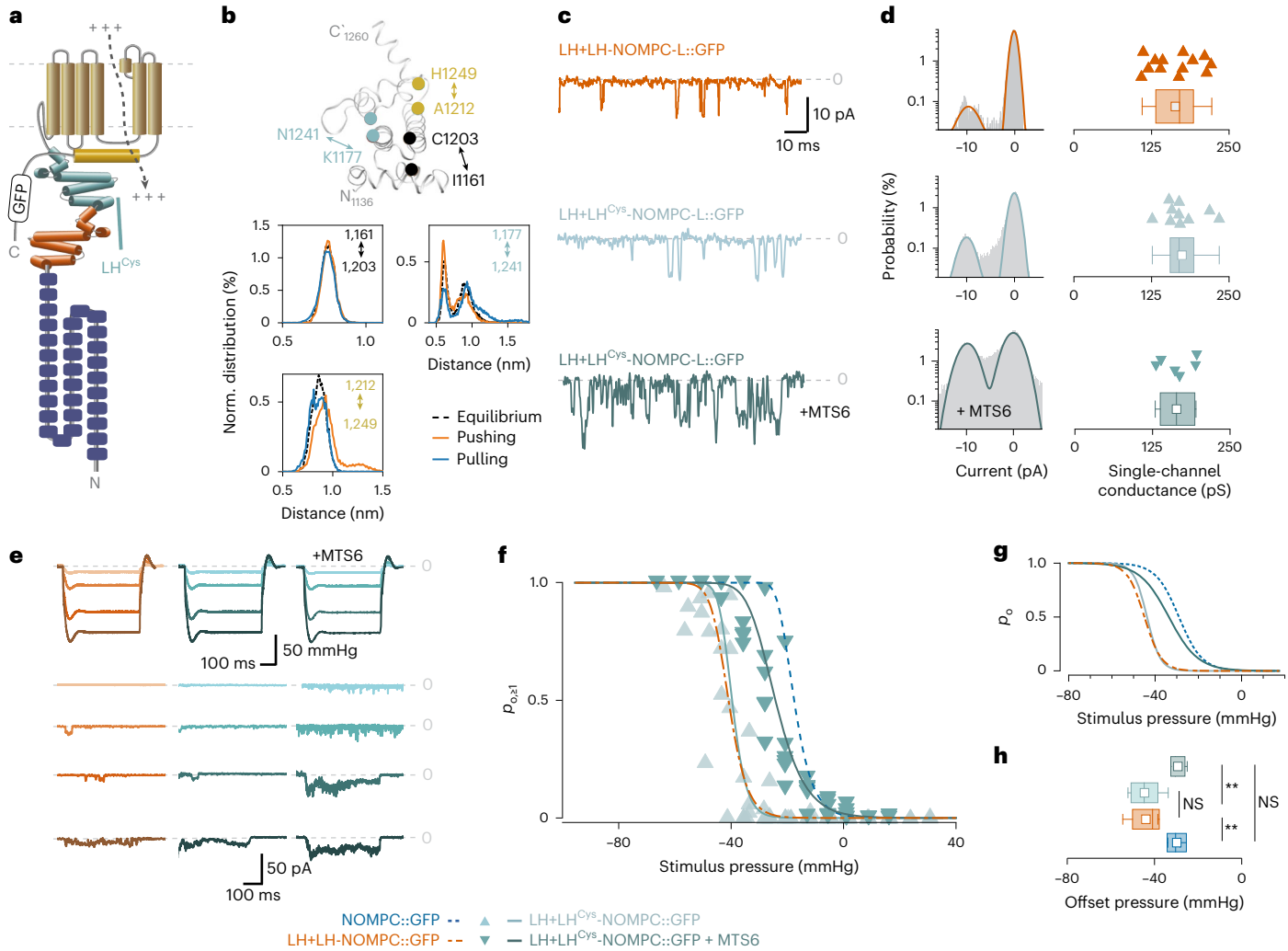

Fig. 5 | Constraining one-half of the duplicated LH domain by crosslinking cysteine pairs reverts it functionally to a single LH domain. a, Sketch of LH+LH^{Cys}-NOMPC::GFP, in which three vicinal aa pairs of the native LH domain are substituted with cysteine pairs, I1161C–C1203, K1177C–N1241C and A1212C–H1249C. **b**, Placement of those amino acid pairs (top) and distances between their alpha carbons (Cα–Cα) in equilibrium (without forcing) and nonequilibrium (with pushing and pulling force) simulations, during the second half (last 50 ns) of the trajectories. Forcing alters the distance distribution of K1177C–N1241C and A1212C–H1249C, but not that of I1161C–C1203. For correlation coefficients between Cα–Cα distances and principal components of the LH domain, see Extended Data Fig. 4. **c**, Representative spontaneous currents recorded in outside–out patches at a holding potential of −60 mV (at least six cells per protein variant). **d**, Respective amplitude histograms, each fitted with two Gaussians (left). Like LH+LH–NOMPC::GFP (top), LH+LH^{Cys}-NOMPC::GFP (middle) displays low spontaneous activity, yet activity increases immediately upon MTS6 application (bottom), resulting in a current amplitude distribution resembling that of NOMPC::GFP (Fig. 1c, top left). Right, Respective single-channel conductance boxplots (box, 50% of data around median; line in box, median; white square, mean; whiskers, 1.5× interquartile range). **e**, Representative pressure-activated currents (at least six cells per protein variant) **f**, Respective probability to find at least one channel open, $p_{o,\geq 1}$, plotted against the stimulus pressure (symbols), fitted with $Y(X) = 1 - (1 - p_o(X))^N$ (lines). **g**, Respective open probabilities, $p_o(X)$, (top) deduced from the fits. The pressure-dependent open probability of LH+LH^{Cys}-NOMPC::GFP matches that of LH+LH–NOMPC::GFP, but, upon addition of MTS6, shifts to the low pressures that activate NOMPC::GFP. **h**, Boxplots of respective offset pressures corresponding to $p_o = 0.5$ (box, 50% of data around median; line in box, median; white square, mean; whiskers, 1.5× interquartile range). Two-tailed Mann–Whitney *U*-tests with Bonferroni correction; $^*P < 0.05$; $^{**}P < 0.01$; $^{***}P < 0.001$ (Extended Data Fig. 5).

function, especially as our experimental data suggests that, under natural conditions, the AR domain is rather stiff (Figs. 1–3).

LH domain duplication reduces mechanosensitivity in vitro

To test experimentally whether the LH domain acts as a gating spring, we duplicated this domain using the *nompC.L-GFP* plasmid[41], yielding an LH+LH–NOMPC::GFP protein with two LH domains arranged in tandem (Fig. 1a). Like NOMPC::GFP, LH+LH–NOMPC::GFP reached the cell surface in S2 cells (Extended Data Fig. 1a), showing spontaneous openings in excised outside–out membrane patches (Fig. 1b). Compared with NOMPC::GFP, the frequency of opening events was reduced for LH+LH–NOMPC::GFP (Fig. 1b,c; left), while the single-channel conductance was unchanged (Fig. 1c; right). Like NOMPC::GFP, LH+LH–NOMPC::GFP responded to negative pressure, although with reduced sensitivity (Fig. 1d). When plotted against the pressure amplitude, the probability to find at least one channel open, $p_{o,\geq 1} = 1 - (1 - p_o)^N$, was shifted towards more negative pressures for LH+LH–NOMPC::GFP compared with NOMPC::GFP (Fig. 1e). This reduced pressure sensitivity was also seen when we deduced the open probability, $p_o(P)$ (Fig. 1f), documenting that the shift of $p_{o,\geq 1}(P)$ cannot be attributed solely to the reduced channel number, N (Extended Data Fig. 1b), but, independent of that number, reports a shift of $p_o(P)$. Judging from the fits, the pressure amplitude corresponding to $p_o = 0.5$ was −45 ± 2 mmHg (mean ± s.e.m.) for LH+LH–NOMPC::GFP—almost twice the respective amplitude obtained for NOMPC::GFP (−28 ± 2 mmHg)

(Fig. 1g and Extended Data Fig. 1c). Duplicating the LH domain thus reduces NOMPC spontaneous activity and mechanosensitivity, whereby the nearly twofold drop in pressure sensitivity might signal Hookean behavior. Duplicating a Hookean gating spring in tandem should reduce displacement sensitivity twofold, yet our in vitro experiments do not show how displacement scales with the stimulus pressure.

LH domain duplication halves mechanosensitivity in vivo

The reduced mechanosensitivity of LH+LH–NOMPC::GFP was also seen in vivo when we analyzed mechanically evoked JO neuron CAP responses. To replace native NOMPC in these neurons with LH+LH–NOMPC::GFP, we expressed a *UAS-LH+LH-nompC::GFP* transgene in the *nompC*^{3} null mutant background using the expression driver *nompC-GAL4*. In JO neurons, LH+LH–NOMPC::GFP localized to the cilium tips (Extended Data Fig. 2). CAP recordings from JO neurons revealed that, compared with NOMPC::GFP, LH-LH–NOMPC::GFP restores JO mechanosensitivity only partially (Fig. 2a,d). The receiver displacement corresponding to the half-maximal CAP amplitude was 2.8 ± 0.2 µm (mean ± s.e.m.; N = 6 animals) for LH-LH–NOMPC::GFP flies, 2.3 times the respective displacement determined for NOMPC::GFP controls (1.2 ± 0.1 µm; N = 6) (Fig. 2e). This circa twofold drop in displacement sensitivity further points to Hookean behavior, with the duplicated LH domain necessitating displacements that are twice as large to mechano-activate NOMPC. In line with this sensitivity drop, the dynamic range of the CAP response widened slightly, although statistically nonsignificant (Fig. 2f), consistent with the larger working range of softer springs. This dynamic range expansion, though seemingly present in vivo, could not be seen in vitro (Fig. 1f), where it might have been concealed entirely by the variability of the response (Fig. 1e).

LH domain duplication halves gating-spring stiffness

In addition to partially restoring the displacement sensitivity of JO neurons, LH+LH–NOMPC::GFP partially restored the NOMPC-dependent gating compliance in the mechanics of the fly's antennal sound receiver (Fig. 3d). For the NOMPC-dependent sensitive channel type, fits of the gating-spring model yielded a force change, z_s, in the gating spring upon channel opening of only 11 ± 1 fN (mean ± s.e.m.), half the value obtained for NOMPC::GFP controls (Fig. 3e and Supplementary Table 1) and wild-type flies (24 ± 1 fN)[31]. This halving of z was specific to the NOMPC-dependent channels; for the less sensitive, NOMPC-independent channel type, the respective force change, z_{ls}, was identical for flies expressing LH+LH NOMPC::GFP and NOMPC::GFP (Supplementary Table 1). The twofold reduction of z_s in LH+LH NOMPC::GFP flies coincided with a drop of the receiver's asymptotic stiffness K_∞, but not its linear stiffness K_{lin} (Supplementary Table 1), reporting a reduction of the combined gating-spring stiffness, K_{GS}. Compared with NOMPC::GFP controls, the combined stiffness of the NOMPC-dependent gating springs, K_{GS_s}, was reduced in flies expressing LH+LH–NOMPC::GFP (Fig. 3f). When normalized to the number of sensitive channels, $K_{GS_s}/N_s = \gamma^2 k_s$ was only 8 ± 3 nN m^{-1} (mean ± s.e.m.), half the value obtained for NOMPC::GFP controls (17 ± 3 nN m^{-1}; Fig. 3g and Supplementary Table 1). Duplicating the LH domain thus halves the effective stiffness, $\gamma^2 k_s$, of the NOMPC-dependent gating springs, and, thus, their spring constant, k_s. The latter conclusion can be drawn because the duplication halved both $\gamma^2 k_s$ (Fig. 3g) and $z_s = \gamma \kappa_s \delta_s$ (Fig. 3e), indicating that it reduces κ_s only, without altering the projection factor γ and the gating swing δ_s. In effect, LH domain duplication also halved the k_s-dependent gating energy ($EG_s = 1/2\, k_s \delta_s^2$) (Fig. 3h), but not the k_s-independent, projected gating swing, δ_s/γ (Fig. 3i).

Extranumeral LH domain can substitute the native one

Halving the spring constant of the gating spring, the duplicated LH domain behaves like two identical Hookean springs that are arranged in series. Judging from this Hookean behavior, the extranumeral LH domain functions like the native LH domain, which seems unexpected given the tight network of intramolecular interactions the native LH domain makes with the adjacent TRP domain[35]. Accordingly, we reasoned that the inserted, extranumeral LH domain should be able to functionally replace the native LH domain if the latter were stabilized by crosslinking. To test this possibility, we substituted three vicinal aa pairs in the native LH domain with cysteine pairs, I1161C–C1203, K1177C–N1241C and A1212C–H1249C (Fig. 5a,b). For the last two pairs, the Cα–Cα distance between their alpha carbons (Cα) changed in our molecular dynamics simulations when force was applied to the ARs (Fig. 5b), whereby stabilizing these pairs should constrain the hinge-like movement of the LH domain (Extended Data Fig. 4). When expressed in *Drosophila* S2 cells, the modified LH+LH^{Cys}-NOMPC::GFP channel resembled the parental LH+LH–NOMPC::GFP channel with respect to its spontaneous activity (Fig. 5c), single-channel conductance (Fig. 5d) and mechanosensitivity (Fig. 5e,f). The crosslinking reagent 1,6-hexanediyl bismethane-thiosulfonat (MTS6, or MTS-6-MTS) entirely abolished the spontaneous activity of LH+LH^{Cys}-NOMPC::GFP, LH+LH–NOMPC::GFP and NOMPC::GFP within 1 min, signaling unspecific crosslinking (Extended Data Fig. 5a). Immediately upon adding MTS6, however, the frequency of spontaneous openings increased transiently for LH+LH^{Cys}-NOMPC::GFP, yielding a current amplitude distribution (Fig. 5d; left) resembling that obtained for NOMPC::GFP (Fig. 1c, left). No such transient increase was observed for LH+LH–NOMPC::GFP, NOMPC::GFP and a control protein, LH+LH$^{Cys\text{-}ctrl}$-NOMPC::GFP, carrying only one cysteine pair, I1161C–C1203, with the two cysteine pairs placed according to our molecular dynamics simulations being reverted to single, unpaired remaining cysteines, K1177C and A1212C (Extended Data Fig. 5a). Crosslinking also transiently increased the pressure sensitivity of LH+LH^{Cys}-NOMPC::GFP (Fig. 5e and Extended Data Fig. 5b), but not of LH+LH–NOMPC::GFP, NOMPC::GFP, and LH+LH$^{Cys\text{-}ctrl}$-NOMPC::GFP (Extended Data Fig. 5b), shifting the open probability towards the low pressure amplitudes that activate NOMPC::GFP (Fig. 5f–h). Although unspecific crosslinking precluded in vivo testing in the fly, this in vitro restoration of sensitive gating indicates that, by constraining the native LH domain, the duplicated LH domain can be reverted functionally to a single LH domain. Apparently, the structural flexibility identified by our molecular dynamics simulations is essential for LH domain function, and the extranumeral LH domain we introduced can take over this function when the native LH domain is stabilized, suggesting functional equivalence.

LH domain hinge constitutes the gating spring

NOMPC forms tetrameric channels whose four AR domains assemble into an AR bundle[29] whose spring constant, κ_{AR}, has been estimated to range between 4 and 22 pN nm^{-1} (refs. 13,42,43). The respective spring constant of the NOMPC gating spring, κ_s, cannot be deduced directly from fits of the gating-spring model, yet when arbitrarily assuming a gating swing δ_s of 4 nm as estimated for the hair cell MET channel[10], the gating energy required to open one NOMPC::GFP channel (Fig. 3h) translates into κ_s = 2 pN nm^{-1} for the gating spring per NOMPC tetramer. Describing the four AR and LH domains per channel as two springs in series whose combined stiffness equals κ_s, one obtains a spring constant of the LH domains, κ_{LH}, between 2.2 pN nm^{-1} (if κ_{AR} = 22 pN nm^{-1}) and 4 pN nm^{-1} (if κ_{AR} = 4 pN nm^{-1}). In the latter case ($\kappa_{AR} = \kappa_{LH}$ = 4 pN nm^{-1}), halving either κ_{AR} or κ_{LH} through domain duplication would reduce κ_s equally by one-third, which is not what our mechanical measurements revealed. In the former case (κ_{AR} = 22 pN nm^{-1} and κ_{LH} = 2.2 pN nm^{-1}), halving κ_{LH} would reduce κ_s by nearly 50% and halving κ_{AR} would lower it by only 9%, which comes closer to the results of our mechanical measurements (Fig. 3). Care seems warranted concerning these absolute stiffness estimates, yet the ratio κ_{LH}/κ_s must be smaller than 1.1 (= 2.2 pN nm^{-1}/2pN nm^{-1}) because κ_s drops by almost exactly 50% upon LH domain duplication, and remains unaltered when the AR domain is duplicated. If the NOMPC gating swing were only 1 nm, the gating energy would translate into a gating-spring stiffness, κ_s, of 31 pN nm^{-1}, indicating a spring constant, κ_{AR}, of the AR bundle of at least 310 pN nm^{-1}

given the mechanical effects observed. Independent of absolute stiffness estimates, the AR domain thus must be at least ten times stiffer than the LH domain, and the LH domain contributes over 90% of the gating-spring compliance, leaving little room for elastic contributions from other coupling elements such as the AR and TRP domains and the cell membrane. Hence, instead of being one of several gating-spring components, the LH domain hinge governs gating-spring mechanics and, accordingly, is the gating spring.

Discussion

This study identifies the NOMPC LH domain as a gating spring that, admitting and promoting gating movements, initiates mechanosensing, showing how efficient gating is achieved. By flexibly suspending gate and TRP domain on the AR domain, the hinge formed by the LH domain allows the gate to switch conformation locally, whereby the gate movements can be organized by the TRP domain. Through its elasticity, the hinge can accommodate gating movements and store their energy, without passing the movements to the stimulus-convening AR domain. This facilitates energy-efficient and fast gating transitions by reducing friction and, thus, sensitive gating by weak stimuli. Because the hinge suspending the gate is the most compliant coupling element, the gating spring, stimuli can be coupled efficiently to the hinge, and gate the channel by deforming the hinge. We anticipate this gating scheme to be universal in that it is realized in many ion channels, irrespective of the nature of the gating stimuli. Actuating channel gates requires force, and many ion channels bear flexible linkers between stimulus-receiving sensor domains and gate[51–53], including, for example, TRPV4, whose linker corresponding to the NOMPC LH domain receives force induced by ligand binding from the AR domain[54]. Several of those linkers couple stimulus-induced conformational changes to channel pore activity and seem to show spring behavior[52,53,55], suggesting that, analogous to the NOMPC LH domain, they might act as gating springs. To allow stimuli to actuate channel gates temporarily, the gate has to be suspended elastically and, to enable efficient gating, this elastic suspension has to be the most compliant coupling element, the gating spring. If a hair cell tip link, the voltage sensor domain of a voltage-gated channel or any other stimulus-conveying structure were more compliant than the gate suspension, stimuli would perform mechanical work on those structures, without moving the gate. Instead of tip links, an intracellular tether formed by the 24 AR protein ankyrin was proposed recently to serve as the hair cell gating spring[25]. Judging from the NOMPC AR domain, however, ankyrin might be too rigid to act as a gating spring, suggesting that that spring is built into the hair cell MET channel complex, suspending the channel gate elastically. Such an arrangement might also be realized in MET channels of the Piezo family, where the short linker element known as the latch could serve as gating spring[56]. So far, gating springs have been associated mainly with tether filaments, as formed by the NOMPC AR domain, and a particular mode of MET channel gating that involves such filaments[1–7,12–14,19–21,23–30,33–39]. By identifying and characterizing the NOMPC gating spring, this study proposes gating springs as core ion channel constituents that enable efficient gating in diverse channels and by diverse stimuli.

Online content

Any methods, additional references, Nature Portfolio reporting summaries, source data, extended data, supplementary information, acknowledgements, peer review information; details of author contributions and competing interests; and statements of data and code availability are available at https://doi.org/10.1038/s41593-024-01849-3.

References

1. Hudspeth, A. J., Choe, Y., Mehta, A. D. & Martin, P. Putting ion channels to work: mechanoelectrical transduction, adaptation, and amplification by hair cells. *Proc. Natl Acad. Sci. USA* **97**, 11765–11772 (2000).
2. Gillespie, P. G. & Walker, R. G. Molecular basis of mechanosensory transduction. *Nature* **413**, 194–202 (2001).
3. Chalfie, M. Neurosensory mechanotransduction. *Nat. Rev. Mol. Cell Biol.* **10**, 44–52 (2009).
4. Kim, M., Heo, G. & Kim, S. Y. Neural signalling of gut mechanosensation in ingestive and digestive processes. *Nat. Rev. Neurosci.* **23**, 135–156 (2022).
5. Delmas, P. & Coste, B. Mechano-gated ion channels in sensory systems. *Cell* **155**, 278–284 (2013).
6. Jin, P., Jan, L. Y. & Jan, Y. N. Mechanosensitive ion channels: structural features relevant to mechanotransduction mechanisms. *Annu. Rev. Neurosci.* **43**, 207–229 (2020).
7. Kefauver, J. M., Ward, A. B. & Patapoutian, A. Discoveries in structure and physiology of mechanically activated ion channels. *Nature* **587**, 567–576 (2020).
8. Cox, C. D., Bavi, N. & Martinac, B. Biophysical principles of ion-channel-mediated mechanosensory transduction. *Cell Rep.* **29**, 1–12 (2019).
9. Corey, D. P. & Hudspeth, A. J. Response latency of vertebrate hair cells. *Biophys. J.* **26**, 499–506 (1979).
10. Corey, D. P. & Hudspeth, A. J. Kinetics of the receptor current in bullfrog saccular hair cells. *J. Neurosci.* **3**, 962–976 (1983).
11. Howard, J. & Hudspeth, A. J. Mechanical relaxation of the hair bundle mediates adaptation in mechanoelectrical transduction by the bullfrog's saccular hair cell. *Proc. Natl Acad. Sci. USA* **84**, 3064–3068 (1987).
12. Howard, J. & Hudspeth, A. J. Compliance of the hair bundle associated with gating of mechanoelectrical transduction channels in the bullfrog's saccular hair cell. *Neuron* **1**, 189–199 (1988).
13. Markin, V. S. & Hudspeth, A. J. Gating-spring models of mechanoelectrical transduction by hair cells of the internal ear. *Annu. Rev. Biophys. Biomol. Struct.* **24**, 59–83 (1995).
14. Sukharev, S. & Corey, D. P. Mechanosensitive channels: multiplicity of families and gating paradigms. *Sci. STKE.* **2004**, re4 (2004).
15. Ricci, A. J., Crawford, A. C. & Fettiplace, R. Mechanisms of active hair bundle motion in auditory hair cells. *J. Neurosci.* **22**, 44–52 (2002).
16. Kennedy, H. J., Crawford, A. C. & Fettiplace, R. Force generation by mammalian hair bundles supports a role in cochlear amplification. *Nature* **433**, 880–883 (2005).
17. Tobin, M., Chaiyasitdhi, A., Michel, V., Michalski, N. & Martin, P. Stiffness and tension gradients of the hair cell's tip-link complex in the mammalian cochlea. *eLife* **8**, e43473 (2019).
18. Albert, J. T., Nadrowski, B. & Göpfert, M. C. Mechanical signatures of transducer gating in the *Drosophila* ear. *Curr. Biol.* **17**, 1000–1006 (2007).
19. Gillespie, P. G., Dumont, R. A. & Kachar, B. Have we found the tip link, transduction channel, and gating spring of the hair cell? *Curr. Opin. Neurobiol.* **15**, 389–396 (2005).
20. Christensen, A. P. & Corey, D. P. TRP channels in mechanosensation: direct or indirect activation? *Nat. Rev. Neurosci.* **8**, 510–521 (2007).
21. Hudspeth, A. J. & Gillespie, P. G. Pulling springs to tune transduction: adaptation by hair cells. *Neuron* **12**, 1–9 (1994).
22. Kachar, B., Parakkal, M., Kurc, M., Zhao, Y. & Gillespie, P. G. High-resolution structure of hair-cell tip links. *Proc. Natl Acad. Sci. USA* **97**, 13336–13341 (2000).
23. Sotomayor, M., Corey, D. P. & Schulten, K. In search of the hair-cell gating spring: elastic properties of ankyrin and cadherin repeats. *Structure* **13**, 669–682 (2005).
24. Gillespie, P. G. & Müller, U. Mechanotransduction by hair cells: models, molecules, and mechanisms. *Cell* **139**, 33–44 (2009).
25. Zheng, W. & Holt, J. R. The mechanosensory transduction machinery in inner ear hair cells. *Annu. Rev. Biophys.* **50**, 31–51 (2021).

26. Caprara, G. A. & Peng, A. W. Mechanotransduction in mammalian sensory hair cells. *Mol. Cell. Neurosci.* **120**, 103706 (2022).
27. Araya-Secchi, R., Neel, B. L. & Sotomayor, M. An elastic element in the protocadherin-15 tip link of the inner ear. *Nat. Commun.* **7**, 13458 (2016).
28. Bartsch, T. F. et al. Elasticity of individual protocadherin 15 molecules implicates tip links as the gating springs for hearing. *Proc. Natl Acad. Sci. USA* **116**, 11048–11056 (2019).
29. Tang, Y. Q. et al. Ankyrin is an intracellular tether for TMC mechanotransduction channels. *Neuron* **107**, 112–125 (2020).
30. Howard, J. & Bechstedt, S. Hypothesis: a helix of ankyrin repeats of the NOMPC-TRP ion channel is the gating spring of mechanoreceptors. *Curr. Biol.* **14**, R224–R226 (2004).
31. Effertz, T., Nadrowski, B., Piepenbrock, D., Albert, J. T. & Göpfert, M. C. Direct gating and mechanical integrity of *Drosophila* auditory transducers require TRPN1. *Nat. Neurosci.* **15**, 1198–1200 (2012).
32. Yan, Z. et al. *Drosophila* NOMPC is a mechanotransduction channel subunit for gentle-touch sensation. *Nature* **493**, 221–225 (2013).
33. Liang, X. et al. A NOMPC-dependent membrane-microtubule connector is a candidate for the gating spring in fly mechano-receptors. *Curr. Biol.* **23**, 755–763 (2013).
34. Zhang, W. et al. Ankyrin repeats convey force to gate the NOMPC mechanotransduction channel. *Cell* **162**, 1391–1403 (2015).
35. Jin, P. et al. Electron cryo-microscopy structure of the mechanotransduction channel NOMPC. *Nature* **547**, 118–122 (2017).
36. Argudo, D., Capponi, S., Bethel, N. P. & Grabe, M. A multiscale model of mechanotransduction by the ankyrin chains of the NOMPC channel. *J. Gen. Physiol.* **151**, 316–327 (2019).
37. Sun, L. et al. Ultrastructural organization of NompC in the mechano-receptive organelle of *Drosophila* campaniform mechanoreceptors. *Proc. Natl Acad. Sci. USA* **116**, 7343–7352 (2019).
38. Hehlert, P., Zhang, W. & Göpfert, M. C. *Drosophila* mechanosensory transduction. *Trends Neurosci.* **44**, 323–335 (2021).
39. Wang, Y. et al. The push-to-open mechanism of the tethered mechanosensitive ion channel NompC. *eLife* **10**, e58388 (2021).
40. Walker, R. G., Willingham, A. T. & Zuker, C. S. A *Drosophila* mechanosensory transduction channel. *Science* **287**, 2229–2234 (2000).
41. Cheng, L. E., Song, W., Looger, L. L., Jan, L. Y. & Jan, Y. N. The role of the TRP channel NompC in *Drosophila* larval and adult locomotion. *Neuron* **67**, 373–380 (2010).
42. Effertz, T., Wiek, R. & Göpfert, M. C. NompC TRP channel is essential for *Drosophila* sound receptor function. *Curr. Biol.* **21**, 592–597 (2011).
43. Powers, R. J. et al. Stereocilia membrane deformation: implications for the gating spring and mechanotransduction channel. *Biophys. J.* **102**, 201–210 (2012).
44. Lee, G. et al. Nanospring behaviour of ankyrin repeats. *Nature* **440**, 246–249 (2006).
45. Besch, S. R., Suchyna, T. & Sachs, F. High-speed pressure clamp. *Pflügers Arch.* **445**, 161–166 (2002).
46. Lee, J., Moon, S., Cha, Y. & Chung, Y. D. *Drosophila* TRPN(=NOMPC) channel localizes to the distal end of mechanosensory cilia. *PLoS ONE* **5**, e11012 (2010).
47. Brand, A. H. & Perrimon, N. Targeted gene expression as a means of altering cell fates and generating dominant phenotypes. *Development* **118**, 401–415 (1993).
48. Nadrowski, B., Albert, J. T. & Göpfert, M. C. Transducer-based force generation explains active process in *Drosophila* hearing. *Curr. Biol.* **18**, 1365–1372 (2008).
49. Veevers, R. & Hayward, S. Methodological improvements for the analysis of domain movements in large biomolecular complexes. *Biophys. Physicobiol.* **16**, 328–336 (2019).
50. Eargle, J. & Luthey-Schulten, Z. NetworkView: 3D display and analysis of protein·RNA interaction networks. *Bioinformatics* **28**, 3000–3001 (2012).
51. Twomey, E. C. & Sobolevsky, A. I. Structural mechanisms of gating in ionotropic glutamate receptors. *Biochemistry* **57**, 267–276 (2018).
52. Cowgill, J. & Chanda, B. Mapping electromechanical coupling pathways in voltage-gated ion channels: challenges and the way forward. *J. Mol. Biol.* **433**, 167104 (2021).
53. Scheuring, S. Forces and energetics of the canonical tetrameric cation channel gating. *Proc. Natl Acad. Sci. USA* **120**, e2221616120 (2023).
54. Goretzki, B. et al. Crosstalk between regulatory elements in disordered TRPV4 N-terminus modulates lipid-dependent channel activity. *Nat. Commun.* **14**, 4165 (2023).
55. Niu, X., Qian, X. & Magleby, K. L. Linker-gating ring complex as passive spring and Ca^{2+}-dependent machine for a voltage- and Ca^{2+}-activated potassium channel. *Neuron* **42**, 745–756 (2004).
56. Young, M., Lewis, A. H. & Grandl, J. Physics of mechanotransduction by Piezo ion channels. *J. Gen. Physiol.* **154**, e202113044 (2022).

Methods

Animal models

Fly (*Drosophila melanogaster*) stocks used in this study and their respective origins are as follows: for *nompC* null mutant background, *+/+;nompC[3],cn[1],bw[1]/CyO;+/+* (BDSC 42258) was used. For rescue experiments, the Gal4/UAS-system[47,57] was used with *+/+;nompC[1]/CyO-WeeP;nompC-Gal4* (ref. 41) for JO neuron expression. For rescue experiments, respective *nompC*-alleles were used: *w[1118];nompC[3],UAS-nompC::GFP/CyO;+/+* (NOMPC::GFP, *this study*), *w*;nompC[1],UAS-29 + 29ARs-nompC::GFP/CyO;+/+* (AR + AR–NOMPC::GFP, gift from Y.-N. Jan) and *w[1118];nompC[3];UAS-nompC[LH+LH-Cys]::GFP* (LH+LH–NOMPC::GFP, this study). Flies were kept at 25 °C, 60% humidity on standard cornmeal–yeast medium in a 12-h/12-h light/dark cycle. *nompC* null mutants were collected as pupae from the culture vials and kept on filter paper soaked with a 1% sucrose solution (in H_2O) to facilitate eclosion[58]. Experiments were performed using adult flies 2–5 days after eclosion, irrespective of their sex because neither JO function nor auditory mechanics seem to be sex-specific. Dealing with an invertebrate species, no ethical approval was needed. Experiments were carried out in accordance with German Federal Regulations (license Gen.Az 501.40611/0166/501).

LH domain duplication

The NOMPC LH domain is ~125 amino acids in length, spanning approximately residues 1136–1260 of NOMPC.L (UniProt A8DYV6_DROME)[35]. To generate LH+LH–NOMPC::GFP, two *nompC* constructs were generated from *pUAST-attB-nompC.L-GFP* (provided by J. N. Jan) by PCR (Phire Tissue Direct PCR Master Mix, Thermo Fisher Scientific, F170S): (1) one N-terminal construct including the AR+LH domain (residue 1–1269, via primers 5′-CCgaattcATGTCGCAGCCGCGCGGAGGGCGT-3′ *nompC-F*-EcoRI-ATG_Fw, 5′-CCagatctGGATGCCCACGTCAGGGAGC CATG-3′ *nompC-LH*^{End}-BglII_Rv) and (2) one C-terminal construct containing the LH domain, the transmembrane core and the GFP-tagged C terminus (residues 1139–*, via primers 5′-GGagatctATGGAGGACAAGC GATTCGTGTACA-3′ *nompC*-LH^{Start}-BglII_Fw / 5′-CCtctagaTTACTTG TACAGCTCGTCCATGCCGAGA-3′ *nompC-eGFP*^{TAA}-XbaI_Rv). By fusing the two constructs (using BglII, *pUAST-attB-nompC[LH+LH]-GFP* (LH+LH–NOMPC::GFP) was generated that includes two LH domains arranged in tandem, one spanning residues 1136–1260 of NOMPC.L and the second spanning aa 1139–1260. Judging from our results, the missing four amino acids (1136–1139) of the latter LH domain do not contribute to domain function, narrowing down the functional domain to approximately 120 amino acids (1139–1260 of NOMPC.L).

To generate LH+LH^{Cys}-NOMPC::GFP, additional cysteines were introduced into the LH domain of construct 2 (see above) using the QuikChange Lightning Multi Site-Directed Mutagenesis Kit (Agilent, 210515) with the primers 5′-GACGTTCTCATTGAATGTGAGCAGAA GGAAGTGATTGCCTGCACGGTAGTTCAGCG-3′ (NOMPC^{N1241C,H1249C}_Fw), 5′-GCCACGGAGCTCTTGTGCCTGGCAGCTGGGTC-3′ (NOMPC^{A1212C}_Fw, 5′-GTGGATACAGCCGCCTGTCTGTCCAACATCTAC-3′ (NOMPC^{K1177C}_Fw), and 5′-CAGGACAAACTCCTGACAGGGCTTGTTGTTGTG-3′ (NOMP C^{I1161C}_Rv), in serial rounds according to the manufacturer protocol (creating construct 3). By fusing this construct 3 to construct 1 (see above), we obtained *pUAST-attB-nompC[LH+LH^{Cys}]::GFP* (note that LH^{Cys} is the native LH domain that interacts directly with TRP and the transmembrane domain, not the extranumeral LH domain that is connected to the AR domain). To create a control for the crosslinking experiments (LH+LH$^{Cys\text{-}ctrl}$-NOMPC::GFP), one cysteine of each of the hinge cysteine-double-pairs was reverted back to C1241N, C1249H through site-directed mutagenesis (see above, primer 5′-CGACGTTCT CATTGAAAATGAGCAGAAGGAAGTGATTGCCCACACGGTAGTTC-3′).

All constructs were confirmed by sequencing. Transgenic flies were generated by BestGene (http://www.thebestgene.com), and the respective constructs were recombined with *nompC[3]* allele. The *nompC[3]* allele was genotyped via PCR (primers 5′-TGCCCTGCTGAC CAATAAG-3′ and 5′-TGACAGACTTCCATCTGCC-3′) and subsequently subjected to restriction digest with FspBI and BfaI. All restriction enzymes used were purchased from Thermo Fisher Scientific (EcoRI, F170S; BglII, FD0083; XbaI, FD0684; FspBI, FD1764).

Heterologous expression in S2 cells

Drosophila S2 cells (ATCC, CRL-1963) were maintained according to the protocol of Harvard Medical School (https://fgr.hms.harvard.edu/fly-cell-culture). For heterologous expression of GFP-tagged NOMPC constructs (Fig. 1 and Extended Data Fig. 1), cells were transfected with Effectene Transfection Reagent (Qiagen, 301425) following the manufacturer's protocol; 500 ng of *pAct5C-Gal4* vector (this study) was cotransfected with an equimolar amount of *pUAST*-vector with the respective *NOMPC::GFP* construct. For the *UAST-NOMPC::GFP*-vectors, freshly generated mini-preps (Macherey Nagel, 740490.250) gave higher transfection yields, especially for *pUAST-attB-nompC[LH+LH]::GFP and pUAST-attB-nompC[AR+AR]::GFP* (also called *pUAST-attB-29+29ARs-NOMPC::GFP*)[34]. Cells were incubated for 2–3 days to allow for protein expression and membrane localization before their transfer to cover slips coated with Concanavalin A (Merck, C5275-5MG). After allowing the cells to sediment and adhere for at least 1 h, cells were used for patch-clamp experiments within a time window of 1–3 h.

Cell surface localization of GFP-tagged NOMPC constructs (Extended Data Fig. 1a) was assessed by total internal reflection microscopy with a Zeiss Axio Observer.Z1 microscope and an Evolve 512 EMCCD camera (Photometrics) and Zen Blue software, using ×63 EC Plan-NEOFLUAR and ×100 α Plan-APOCHROMAT objectives.

In vitro patch-clamp recordings

We recorded currents of NOMPC channel constructs with fire-polished patch pipettes (WPI, 1B150F-4) of 2–3.5 MΩ at 30 kHz (with digital postprocessing filtering at 2 kHz) with a HEKA EPC10 amplifier (HEKA Elektronik GmbH). Intracellular patch solution consisted of 140 mM cesium methanesulfonate (Sigma-Aldrich, C1426-5G) and 10 mM HEPES (Sigma-Aldrich, H4034-100G), while the extracellular solution contained 140 mM sodium methansulfonate (Sigma-Aldrich) and 10 mM HEPES. All solutions were adjusted to pH 7.2 (with either CsOH (Sigma-Aldrich, C8518-10G) or NaOH) and to 320 mOsm (with cesium methanesulfonate and sodium methanesulfonate, respectively). All recordings were performed in voltage clamp mode at −60 mV. Cells were imaged on an Examiner.D1 with a ×40 dipping objective (Zeiss), using a light source (Zeiss HXP120 C) and a fluorescein isothiocyanate filter to identify GFP-positive cells. Cells were first patched in whole-cell configuration. Cells with a leak current >50 pA were discarded, as were cells with a series resistance (R_S) > 20 MΩ. The presence of spontaneous current events was established in whole-cell configuration, before switching to an outside–out patch configuration for the remainder of the experiment. Spontaneous current events were then recorded in outside–out cell patches before the same patches were stimulated using a high-speed-pressure-clamp system (HSPC-2-SB, Ala Scientific Instruments) controlled by the HEKA EPC10 (HSPC-2-SB) and the Patchmaster software (HEKA, v.2x90.2). Stimuli of −80 to +20 mmHg were applied and recorded from the monitor port of the HSPC system. Data analysis used the monitor signals to define stimulus amplitudes, which were determined in their stable state, after an initial peak. Python, Clampfit (Molecular Devices), Excel (Microsoft) and Origin Pro 2020 (OriginLab) were used for postprocessing and data analysis. We assume that each outside–out patch includes N identical channels, and that the number N varies between patches. We further assume that each individual channel has an open probability, p_o, that is determined by the external pressure P applied to the patch. This open probability p_o is considered to be identical for the individual channels in the membrane patch, determined by the external pressure P: $p_o(P)$. The Bernoulli distribution then allows us to assess the single-channel

open probability $p_o(P)$ by determining the probability to find at least one channel open, $p_{o,\geq 1}$: $p_{o,\geq 1} = 1 - (1 - p_o)^N$. To rule out artefacts due to adaptation, we restricted the analysis to a time window of 500 ms, beginning 100 ms after stimulus onset. Upon correcting for baseline drift, we determined $p_{o,\geq 1}$ by assigning a 1 to each datapoint in that time window when its current amplitude reached that of a single current event (based on spontaneous events for each patch), or a 0 when its current amplitude was below that of single events. Zeros and ones were summed up for the entire time window and divided by the number of datapoints, yielding $p_{o,\geq 1}$, which can assume values between 0 (current amplitudes never reached that of a single event) and 1 (current amplitudes always reached or exceed it). We then plotted $p_{o,\geq 1}$ against the pressure amplitude P (Fig. 1e). By fitting this pressure-dependent probability, $p_{o,\geq 1}(P)$, with $Y(P) = 1 = 1 - (1 - p_o)^N$, we deduced p_o (Fig. 1f) and the channel number, N (Extended Data Fig. 1b). To assess the validity of the fits, we independently estimated the channel number by diving the peak current $I_{max} = N_i$ by the single-channel current i (Extended Data Fig. 1b), and normalized the pressure-dependent current amplitude $I(P) = N_i p_o(P)$ to the maximum current amplitude I_{max} (Extended Data Fig. 1c).

Localization of NOMPC constructs in JO neurons

Localization of recombinantly expressed GFP-tagged proteins or endogenous NOMPC was visualized in fixed adult JO tissue sections (Extended Data Fig. 2). Staining was performed as described[59,60]. In brief, fly antennal second sections were prepared from 5-day adult fly heads. Heads of adult flies, 5 days posteclosure, were isolated and fixed in 4% paraformaldehyde (Merck) for 1 h at room temperature. After a brief wash with 1× PBS (Merck, P4417) heads were embedded in albumin gelatine and fixed in 6% paraformaldehyde, 0.3% PBS-T (Triton, Sigma-Aldrich, X100), pH 7.4, at 4 °C overnight. The embedded heads were then fixed in 100% methanol (Merck) for 10 min at 4 °C and quickly transferred to 1× PBS for rehydration. Tissue sections (40 µm) were generated with a microtome, and tissue slices were stored in 1× PBS-T. Samples were blocked in blocking buffer (1× PBS-T, 5% normal goat serum, 2% bovine serum albumin) for 1 h at room temperature. Tissues were then incubated with FluoTag-X4 Atto 488 nm anti-GFP (1:1,000, NanoTag Biotechnologies, N0304) and Cy3-conjugated goat anti-HRP (1:300, Jackson ImmunoResearch, 123-165-021) in blocking buffer for 2 h at room temperature. After three washing steps with 1× PBS-T (10 min, room temperature), tissue samples were mounted on microscope slides in DABCO (Carl Roth, 0718.1). For NOMPC staining, samples were treated as described above with the exception that tissues were incubated with rabbit anti-NOMPC-EC (provided by Y.-N. Jan, 1:500, in blocking buffer) for one night at 4 °C. After three washing steps with 1× PBS-T (10 min, room temperature) tissue samples were incubated with Alexa Fluor 488 goat anti-rabbit (in blocking buffer, 1:1,000, Thermo Fisher Scientific, A-11008) for 2 h at room temperature and then washed and mounted as described above.

Stainings were analyzed with a Leica SP8 microscope (at 20 °C) in 8-bit mode using a C-Apochromat ×63/1.40 W Korr FCS M27 objective and Leica X software. For fluorescence detection, the following settings were used: Atto 488/Alexa-488 (excitation, 488 nm; emission, 490–540 nm); Cy3 (excitation, 561 nm; emission, 566–610 nm). Images were subsequently processed in Image J v.1.49 m (National Institutes of Health) and arranged in Adobe Illustrator Creative Cloud and InDesign Creative Cloud.

JO neuron CAP responses

CAP responses of JO neurons were recorded extracellularly as described[18,61], using an electrolytically tapered tungsten wire inserted into the joint between antenna and head capsule. A second tungsten wire inserted into the thorax beneath the scutellum served as indifferent electrode. CAP responses were evoked by actuating the antennal sound receiver electrostatically with force steps (duration 60 ms)[18,31]. Force steps were imposed by feeding voltage commands of opposing sign to two tungsten stereotrodes (Micro Probe (back) WE3ST31.0A5, (front) WE3ST31.0A10) placed equidistantly in front and behind the sound receiver. To allow each stereotrode to push and pull the antenna back and forth, the fly's electrical potential was lifted to around 100 V against ground via the indifferent electrode[18]. Force steps of different amplitude were presented in a randomized order, whereby each amplitude was presented around 100 (large amplitudes) to 10,000 (small amplitudes) times. Simultaneously with the CAP recordings, the displacement of the antennal sound receiver was monitored near the tip of the antennal arista using a Polytec PSV-400 scanning laser Doppler vibrometer equipped with a DD-500 displacement decoder (Polytec, Polytec Acquisition software v.9.4). Command voltages, electrode signals and displacement signals were sampled at a rate of 100 kHz for offline analysis using Spike v.2 (CED). To extract CAP and displacement amplitudes, CAP and displacement responses to identical forcing amplitudes were averaged, and the amplitudes of the initial peak of the CAP response and the corresponding receiver displacement were determined.

Gating compliance measurement and modeling

To assess the gating compliance in the mechanics of the fly's antennal sound receiver, the displacement response of the receiver to force steps was measured as described above. Following previous studies[18,31,48] the external force, $F = m\ddot{X}_{onset}$, experienced by the antennal receiver was calculated from the receiver's maximum acceleration upon forcing onset, $\ddot{X}_{max}$, and its apparent mass, m (~5×10^{-9} g)[18]. The dynamic stiffness of the receiver, $\partial m\ddot{X}_{onset}/\partial X_{peak}$, was calculated for the peak displacement, X_{peak} upon forcing onset, and the steady-state stiffness, $\partial m\ddot{X}_{onset}/\partial X_{steady}$, was determined for the steady-state displacement, X_{steady}, the receiver approached during prolonged forcing, which was extrapolated with exponential fits[18,31,48].

In line with previous work[18,31,48], we describe the receiver's dynamic stiffness with a symmetric gating-spring model that includes opposing channel populations with a displacement-dependent open probability $p_o(X) = 1/(1 + e^{-z(x-x_0)/(k_B T)})$ Each population includes $N/2$ channels, whereby the opposing channel populations have an inversed open probability, $p_o(X)$ and $p_o(-X) = 1 - p_o(X)$. Describing the dynamic stiffness of the receiver in wild-type flies necessitates a gating-spring model with two different, NOMPC-dependent sensitive (s) and NOMPC-independent, less sensitive (ls) channel types[31]. After correcting for inertial effects, the respective displacement-dependent dynamic stiffness of the receiver[31] can be written as

$$K(X) = K_{GS} + K_{lin} - \left(\frac{N_s z_s^2}{k_B T}\right) p_{o_s}(1 - p_{o_s}) - \left(\frac{N_{ls} z_{ls}^2}{k_B T}\right) p_{o_{ls}}(1 - p_{o_{ls}}). \quad (1)$$

$K_{GS} = K_{GS_s} + K_{GS_{ls}}$ is the combined gating stiffness the two channel types together contribute to the mechanics of the fly's antennal receiver, and K_{lin} is the linear stiffness of the receiver (Fig. 3a), which equals the steady-state stiffness because adaptation is complete[18,48]. K_{GS} can be deduced from the difference between the asymptotic stiffness, K_∞, the receiver approaches at large-amplitude displacements (Fig. 3a) and its linear stiffness, $K_{GS} = K_\infty - K_{lin}$ (refs. 12,18). The parameter $z = \gamma\kappa\delta$ denotes the change in force in the gating spring when the respective channel opens[12–14], where γ is a geometric projection factor relating receiver displacements to molecular displacements, κ is the spring constant of the gating spring and δ is the gating swing, that is, the distance by which the gating spring relaxes upon channel opening[12].

In *nompC* null mutants lacking the sensitive, NOMPC-dependent channel type, equation (1) simplifies to

$$K(X) = K_{GS_{ls}} + K_{lin} - \left(\frac{N_{ls} z_{ls}^2}{k_B T}\right) p_{o_{ls}}(X)(1 - p_{o_{ls}}(X)), \quad (2)$$

allowing us to deduce the combined stiffness, $K_{GS_{ls}}$, of the NOMPC-independent gating springs[44].

To assess which of the two equations (equations (1) or (2)) better describes the dynamic receiver stiffness in flies expressing NOMPC::GFP, AR+AR–NOMPC::GFP, or LH+LH–NOMPC::GFP, we fitted the two equations to the pooled data of each strain and determined the sum of the squared residuals, Rss. The goodness of the fits was then assessed using the Akaike information theorem with correction of finite sample size, AICc = AIC + $(2k(k+1)/(n-k-1))$ with AICc = $n\ln(\mathrm{Rss}/n) + 2k$, where k and n are the numbers of free parameters and datapoints, respectively[31].The differences $\Delta = \mathrm{AIC_r} - \mathrm{AICc_{min}}$ of the $r = 2$ models were then used to determine their Akaike weights, $w_i = \exp(-\Delta_i/2)/\sum_{r=1}^{2}\exp(-\Delta_i/2)$, which can range between 0 (probability low) and 1 (probability high) (Supplementary Table 1). For *nompC* null mutants, equations (1) and (2) yielded virtually identical values for w_i, yet equation (2) fit the data better when we clamped z_i to 3 fN—the average value equally obtained for wild-type flies[31] and flies expressing NOMPC::GFP, AR+AR–NOMPC::GFP, and LH+LH–NOMPC::GFP (Supplementary Table 1). For all those latter flies, equation (1) better described the data, as witnessed by larger values of w_i (Supplementary Table 1).

Using the average value of $K_{\mathrm{GS_{ls}}}$ obtained for *nompC* null mutants (17 μM m^{-1}), the combined stiffness of the NOMPC-dependent gating springs, $K_{\mathrm{GS_s}} = K_{\mathrm{GS}} - K_{\mathrm{GS_{ls}}} = N_s\gamma^2 k_s$, was determined for flies expressing the different NOMPC constructs (Fig. 3f). Because γ is not known, the spring constant, k_s, of a NOMPC-dependent gating spring could not be accessed directly, yet what was accessible is its effective stiffness, $\gamma^2 k_s = K_{\mathrm{GS_s}}/N_s$, as seen in the receiver's mechanics (Fig. 3g), the energy required to open the channel, $E_{\mathrm{G_s}} = 1/2k_s\delta_s^2 = 1/2(N_s Z_s^2/K_{\mathrm{GS_s}})$[43] (Fig. 3h) and the projected gating swing, $\delta_s/\gamma = 2E_{\mathrm{G_s}}/z_s$ (Fig. 3i).

Molecular dynamics simulations and analysis

Based on the reported NOMPC structure[35], we extracted a selected part of the protein for molecular dynamics simulations, to enable simulation at the atomistic level. To investigate the protein conformational changes under external force, we performed both equilibrium and nonequilibrium simulations of a truncated version of NOMPC. Specifically, the NOMPC with the whole transmembrane portion, the LH domain and five AR domains was embedded in a 1-palmitoyl-2-oleoyl-*sn*-glycero-3-phosphocholine (POPC) bilayer and 100 ns simulations were performed with and without applied force. In the nonequilibrium simulations, both pulling and pushing forces were applied, respectively, on the center of mass of AR25 (Fig. 4a) with a pulling/pushing rate of 1.5×10^{-5} nm ps^{-1} and a force constant of 5,000 kJ mol nm^{-2}). The final systems contained ~550,000 atoms, including the truncated NOMPC protein, 608 POPC lipids and ~140,000 water molecules. Three parallel simulations were performed for each setup (that is, equilibrium, pulling and pushing simulations; Supplementary Table 2).

Conformations of the LH domain and the AR domains in the simulations were extracted and their RMSDs relative to the reported cryogenic electron microscopy structure were calculated. PCAs were conducted for a truncated part of the protein (addressed as core protein) and the LH domain alone, respectively, to recognize their collective motions during the simulations with and without external force. The former truncated part included the AR domains, the LH domain and part of the transmembrane domain (TRP domain and S5 and S6 helices) (see Figs. 1a and 4a for nomenclature). PCA was performed based on the conformations from all of the trajectories (that is, equilibrium, pulling and pushing simulations). PCAs were conducted after structural superimposition of each of the four subunits of the channel, and motions along the first one or three eigenvectors were examined for the core protein and the LH domain, respectively. In addition, the extreme conformations of the collective motions were subjected to dynamic domain analysis using the DynDom program[49] to identify the hinge region responsible for the rigid body motion described by the eigenvectors. Community network analyses were performed for the core protein using the Networkview tool[50] to investigate the information flow between the AR domains and the TRP helices. Similar to PCA, the community network analyses were conducted after structural superimposition of each of the four subunits of the channel.

To estimate the elasticities of LH domain and ARs, we constructed two simulation systems: (1) the above-mentioned truncated NOMPC with five ARs embedded in a POPC bilayer (Extended Data Fig. 3), and (2) a truncated NOMPC with the LH domain and 26 ARs (AR4–AR29; Extended Data Fig. 3). These systems are addressed as TMD + LH+5AR and LH+26ARs, respectively. For the LH+26ARs system, the missing residues in the experimental structure were added by the FASPR online service[62]. AR1–AR3 were not included as unwinding of their secondary structure was observed in our simulations. For each system, we conducted simulations both without force and with constant forces (both pulling and pushing) applied on the center of mass of a selected AR. We then calculated the force (F)-induced length-change of the LH domain and the ARs together (TMD + LH+5ARs) or only the AR domains (LH+26ARs) along the membrane normal, Δx, to estimate spring constants, $k = F/\Delta x$. In these simulations, we restrained the atomic positions of part of the protein, so that the calculated differences in length (Δx) induced by external force can be ascribed solely to the conformational changes of LH domain or ARs. For the simulations of TMD + LH+5ARs, the spring constant of the LH domain + AR25–AR29 was calculated, with forces (Extended Data Fig. 3) applied on the center of mass of AR25 and the positions of S6 and TRP helices restrained. For the simulations of LH+26ARs, the spring constants of AR4–AR29 and AR25–AR29 were calculated, with forces applied on the centers of mass of AR4 and AR25, respectively. The positions of the LH domain were restrained in these simulations. Three 100 ns parallel simulations were performed for each setup, whereby the last 50 ns trajectories were used to calculate the length of LH domain and AR domains. The accumulated simulation time for this work is ~5.1 μs. The simulations performed in this work are summarized in Supplementary Table 2.

CHARMM-GUI[63] was used to construct the systems, and the molecular dynamics simulations were performed using the GROMACS2019 (ref. 64) software package employing the CHARMM36m force field[65] and the TIP3P water model[66] with an integration time step of 2 fs. We maintained the temperature of the systems at 310 K by the Nose-Hoover thermostat[67,68] with a relaxation time of 1 ps, whereas the pressure was restrained at 1 bar using the semi-isotropic Parrinello-Rahman barostat[69,70] and a relaxation time step of 5 ps; van der Waals interactions were switched off from 1.0 nm to 1.2 nm using the force-switching method[71]. A real space cutoff of 1.2 nm and the particle mesh Ewald method[72,73] were applied to calculate the long-range electrostatic interactions with a Fourier grid spacing of 0.12 nm and an interpolation order of 4 for the Ewald mesh.

Statistics and reproducibility

No statistical methods were used to predetermine sample sizes but our sample sizes are similar to those reported in previous publications[18,31,34,42,48]. Experiments were randomized with respect to genotypes and stimulation amplitudes. No data were excluded from the analyses, except for patch recordings when experiments were incomplete because the patch had ruptured during the experiments. Investigators were blinded initially for genotypes during experiment and outcome assessment, yet blinding was given up in the course of the study because it turned out to be ineffective as genotypes could be inferred easily from phenotypes. To test for statistical differences, two-tailed Mann–Whitney U-tests were used with Bonferroni correction for multiple testing. Descriptive data is presented as mean ± s.e.m. unless stated otherwise. All boxplots are displayed as follows: minimum and maximum are the smallest and largest values, respectively, excluding outliers and the box is drawn from the 25th to 75th percentile with the median in the center. Numbers of biological replicates are indicated in the figure legends. P values less than 0.05 were considered as statistically significant and depicted as follows: $^*P < 0.05$; $^{**}P < 0.01$;

***$P < 0.001$. Representative images of NOMPC construct localization in S2 cells and JO neurons are shown from at least $n = 100$ cells per construct and three flies per strain, respectively.

Reporting summary

Further information on research design is available in the Nature Portfolio Reporting Summary linked to this article.

Data availability

Source data can be found in a public repository[74]. Plasmids and flies generated in this study will be provided on request. The NOMPC.L structure used for the molecular dynamic simulations is accessible at Protein Data Bank (PDB) with accession 5VKQ. Source data are provided with this paper.

References

57. Bischof, J., Maeda, R. K., Hediger, M., Karch, F. & Basler, K. An optimized transgenesis system for *Drosophila* using germ-line-specific phiC31 integrases. *Proc. Natl Acad. Sci. USA* **104**, 3312–3317 (2007).
58. Eberl, D. F., Hardy, R. W. & Kernan, M. J. Genetically similar transduction mechanisms for touch and hearing in Drosophila. *J. Neurosci.* **20**, 5981–5988 (2000).
59. Karak, S. et al. Diverse roles of axonemal dyneins in *Drosophila* auditory neuron function and mechanical amplification in hearing. *Sci. Rep.* **5**, 17085 (2015).
60. Zanini, D. et al. Proprioceptive opsin functions in *Drosophila* larval locomotion. *Neuron* **98**, 67–74 (2018).
61. Eberl, D. F. & Kernan, M. J. Recording sound-evoked potentials from the *Drosophila* antennal nerve. *Cold Spring Harb. Protoc.* **2011**, prot5576 (2011).
62. Huang, X., Pearce, R. & Zhang, Y. FASPR: an open-source tool for fast and accurate protein side-chain packing. *Bioinformatics* **36**, 3758–3765 (2020).
63. Jo, S. et al. CHARMM-GUI 10 years for biomolecular modeling and simulation. *J. Comput. Chem.* **38**, 1114–1124 (2017).
64. Abraham, M. J., Murtola, T. & Lindahl, E. GROMACS: high performance molecular simulations through multi-level parallelism from laptops to supercomputers. *SoftwareX* **1–2**, 19–25 (2015).
65. Huang, J. et al. CHARMM36m: an improved force field for folded and intrinsically disordered proteins. *Nat. Methods* **14**, 71–73 (2017).
66. Jorgensen, W. L., Chandrasekhar, J., Madura, J. D., Impey, R. W. & Klein, M. L. Comparison of simple potential functions for simulating liquid water. *J. Chem. Phys.* **79**, 926–935 (1983).
67. Nosé, S. A unified formulation of the constant temperature molecular dynamics methods. *J. Chem. Phys.* **81**, 511–519 (1984).
68. Hoover, W. G. Canonical dynamics: equilibrium phase-space distributions. *Phys. Rev. A* **31**, 1695–1697 (1985).
69. Parrinello, M. & Rahman, A. Polymorphic transitions in single crystals: a new molecular dynamics method. *J. Appl. Phys.* **52**, 7182–7190 (1981).
70. Nosé, S. & Klein, M. L. Constant pressure molecular dynamics for molecular systems. *Mol. Phys.* **5**, 1055–1076 (1983).
71. Steinbach, P. J. & Brooks, B. R. New spherical-cutoff methods for long-range forces in macromolecular simulation. *Comput. Chem.* **15**, 667–683 (1994).
72. Darden, T., York, D. & Pedersen, L. Particle mesh Ewald: An N·log(N) method for Ewald sums in large systems. *J. Chem. Phys.* **98**, 10089–10092 (1993).
73. Essmann, U. et al. A smooth particle mesh Ewald method. *J. Chem. Phys.* **103**, 8577–8593 (1995).
74. Hehlert, P. et al. NOMPC gating spring - data repository. *Göttingen Research Online* https://doi.org/10.25625/LVUTCE (2024).

Acknowledgements

We thank Y.-N. Jan and L. Jan for providing *nompC.L* and *AR+AR-nompC.L* plasmids, *UAS-AR+AR-nompC.L* and an anti-NOMPC antibody. C. Dean helped with TIRF microscopy, and S. Pauls and N. Schwedthelm-Domeyer provided technical assistance. This study was supported by the German Science Foundation (grants SFB 889 A1, SPP1680, GO 1092/1-2) to M.C.G. and the Cluster of Excellence MBExC (B.L.d.G. and M.C.G.).

Author contributions

M.C.G. initiated this work. P.H. performed molecular biology and cell transfections and ran all the in vivo experiments together with T.E. T.E. performed in vitro patch-clamp recordings and analyzed experimental data together with P.H., B.N., B.R.H.G., D.B. and M.C.G. R.-X.G. and B.L.d.G. carried out and analyzed molecular dynamics simulations. M.C.G. wrote the manuscript together with P.H., T.E., R.-X.G, B.N., D.B. and B.L.d.G., and all authors commented on it and all results.

Competing interests

The authors declare no competing interests.

Additional information

Extended data is available for this paper at https://doi.org/10.1038/s41593-024-01849-3.

Supplementary information The online version contains supplementary material available at https://doi.org/10.1038/s41593-024-01849-3.

Correspondence and requests for materials should be addressed to Martin C. Göpfert.

Peer review information *Nature Neuroscience* thanks the anonymous reviewer(s) for their contribution to the peer review of this work.

https://doi.org/10.1038/s41593-024-01849-3

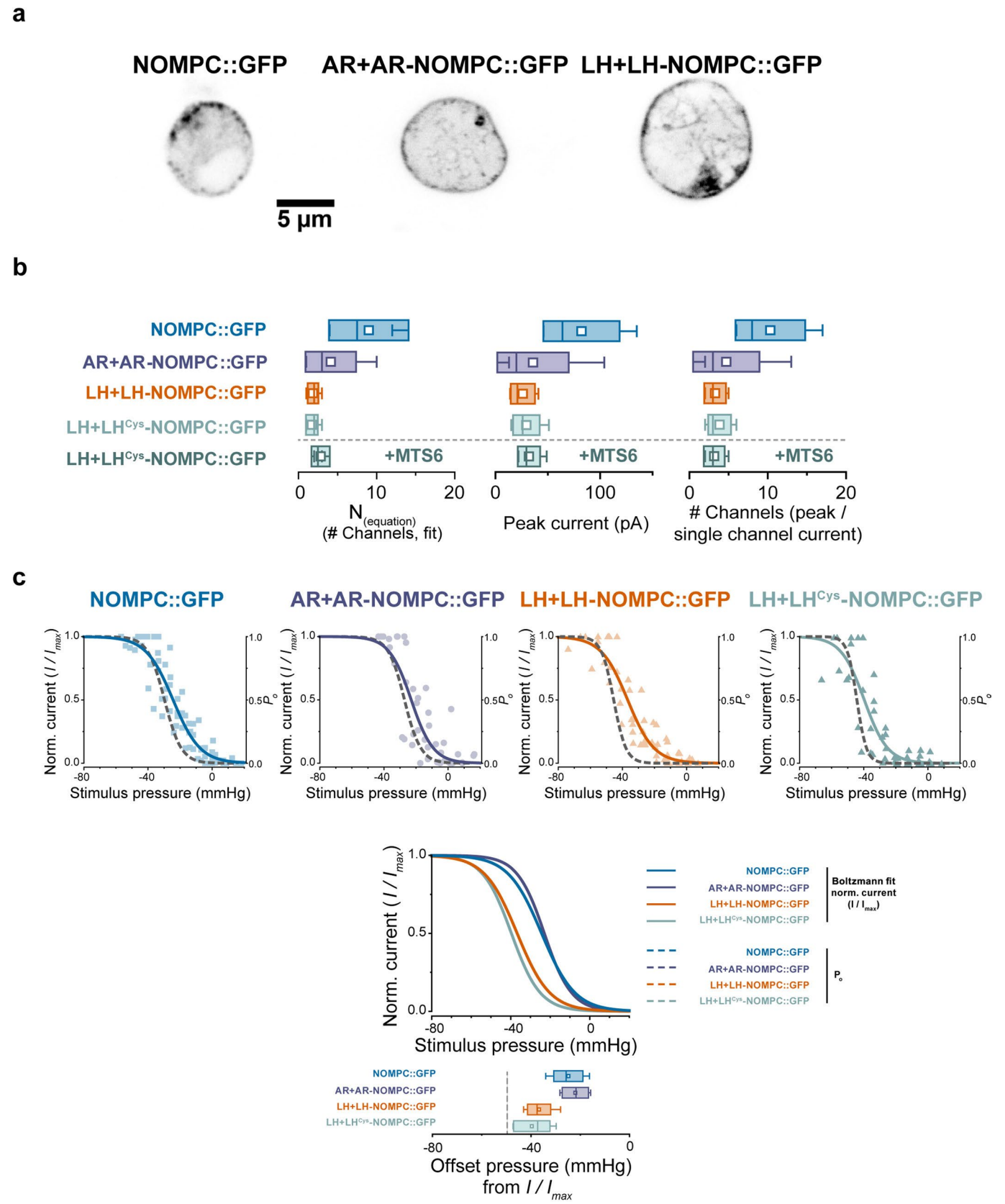

Extended Data Fig. 1 | See next page for caption.

https://doi.org/10.1038/s41593-024-01849-3

Extended Data Fig. 1 | Expression of GFP-tagged NOMPC variants in *Drosophila* S2 cells. a, Protein localization. GFP fluorescence reports cell surface localization for all three variants. n ≥ 100 cells/construct. **b**, Currents and respective channel numbers in excised outside-out membrane patches. Left: channel number N per patch deduced by fitting $p_{o,\geq 1}(P)$ (Fig. 1h) with $Y(P) = 1 - (1 - p_o(P))^N$. Middle: respective peak current amplitudes. Right: channel number deduced by dividing the peak current (middle) by the respective single channel current amplitude (Fig. 1d) (n = (n = 7 cells per protein variant except for n = 9 (NOMPC::GFP) and n = 6 (LH+LH^{Cys}-NOMPC::GFP)). Both methods yield similar channel numbers. **c**, Top: respective normalized amplitudes (I/I_{max}) as function of the stimulus pressure (n = 7 cells per protein variant except for n = 9 (NOMPC::GFP) and n = 6 (AR + AR-NOMPC::GFP)). Solid lines: respective Boltzmann fits. Hatched lines: $p_o(P)$ deduced from Fig. 1f by fitting $p_{o,\geq 1}(P)$ with $Y(P) = 1 - (1 - p_o(P))^N$. Bottom: superimposed Boltzmann fits from the top panels and respective offset pressure corresponding to half-maximal current amplitude (shown for $p_o(P)$ in Fig. 1g). Compared to the deduced $p_o(P)$, the normalized current amplitudes increase less steeply with the stimulus pressure (top), yet, like $p_o(P)$, they superimpose for AR + AR-NOMPC::GFP and NOMPC::GFP and are shifted to approximately twice larger pressures for LH + LH-NOMPC::GFP and LH+LH^{Cys}-NOMPC::GFP.

https://doi.org/10.1038/s41593-024-01849-3

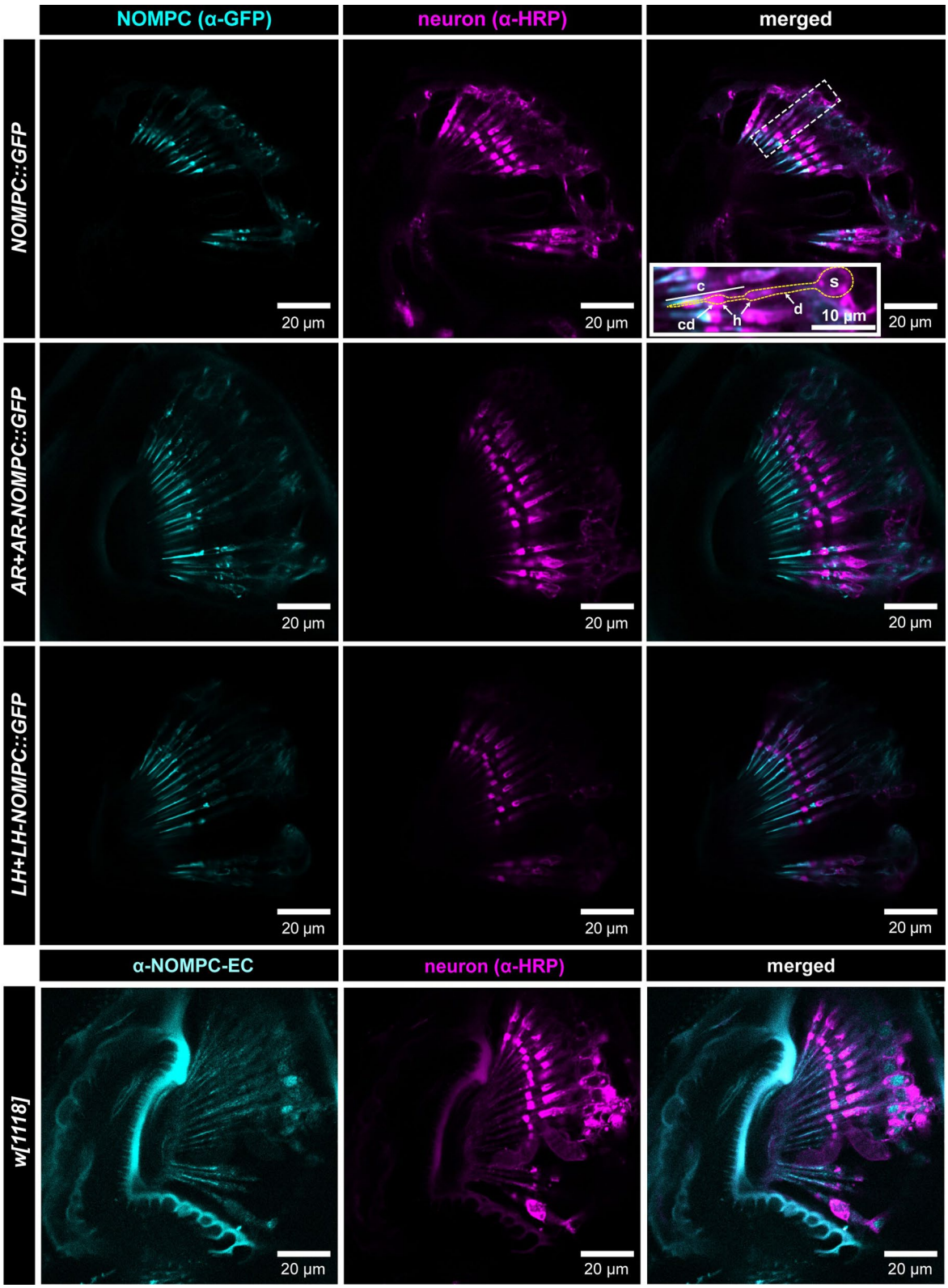

Extended Data Fig. 2 | Localization of GFP-tagged NOMPC variants in *Drosophila* JO neurons. GFP signals are enhanced with an anti-GFP antibody (cyan), and JO neurons are counterstained with anti-horseradish peroxidase (HRP), which recognizes sugar residues of glycoproteins that are secreted by JO neurons in two bands (h, see inset upper right). The proximal band (arrowhead) demarks the junction between the cilium (c) and the dendritic inner segment (d), and the distal band demarks the ciliary dilation ("cd") that separates cilium tip and base regions. s: Cell soma. Anti-GFP staining shows that NOMPC::GFP, AR + AR-NOMPC::GFP, and LH + LH-NOMPC::GFP localize to the cilium tip regions, same as native NOMPC (lower panel, stained with the anti-NOMPC antibody αNOMPC-EC[16]. Scale bars: 20 μm. n = 3 flies/strain.

https://doi.org/10.1038/s41593-024-01849-3

a

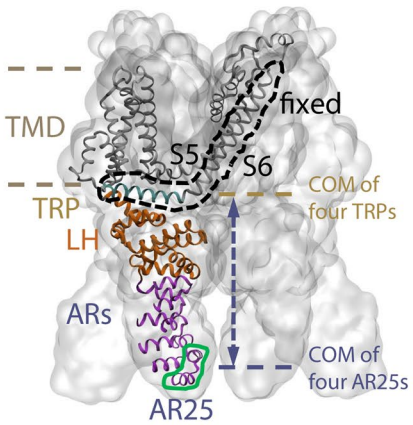

	force (kJ/(mol nm))	spring constant (pN/nm)
pulling	30	126±12
	60	144±19
pushing	-30	155±86
	-60	177±63

b

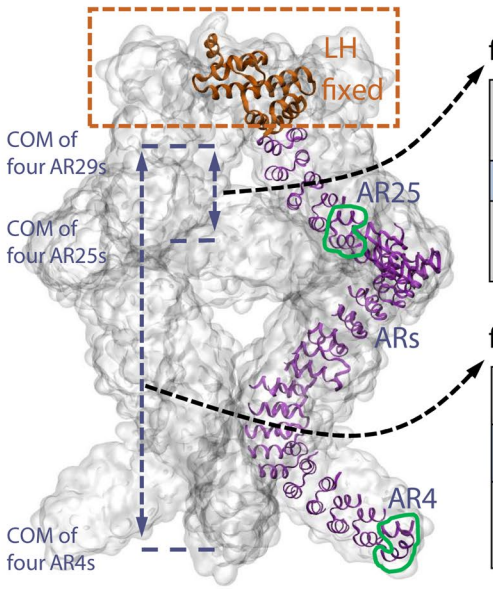

force applied to AR25

	force (kJ/(mol nm))	spring constant (pN/nm)
pulling	60	3020±1372
pushing	-30	1780±127
	-60	3020±274

force applied to AR4

	force (kJ/(mol nm))	spring constant (pN/nm)
pulling	20	115±3
	30	79±16
pushing	-10	39±8
	-20	62±22
	-30	63±1

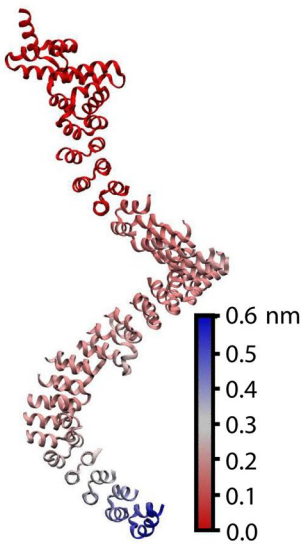

Extended Data Fig. 3 | Elasticities of LH and AR domains. We simulated two systems separately to calculate the spring constants of the LH+5ARs (**a**, TMD + LH+5ARs) and the ARs (**b**, LH+26ARs). Only one subunit is shown in ribbon for clarity, with the transmembrane domain (TMD), the TRP helix, the LH domain and the ARs in gray, cyan, orange and magenta. The ARs on which forces were applied are labelled by green lines. For panel b, we also show the structure of a subunit, which is coloured based on the root-mean-square-fluctuation (RMSF) of the Cα atom of each residue (simulations with a force of 30 kJ/(mol nm) applied to AR4 are used as an example). For additional information, see Methods and Supplementary Table S2.

https://doi.org/10.1038/s41593-024-01849-3

Equilibrium simulations

Dist.	LH	PC1	PC2	PC3
	I1161-C1203	-0.11	0.18	0.20
	K1177-N1241	0.41	0.29	0.49
	A1212-H1249	-0.37	0.12	-0.28
	Q1225-H1261	-0.18	0.48	-0.06

Pushing simulations

Dist.	LH	PC1	PC2	PC3
	I1161-C1203	-0.06	-0.04	0.18
	K1177-N1241	0.63	0.47	0.01
	A1212-H1249	-0.56	-0.35	0.30
	Q1225-H1261	0.09	0.15	0.08

Pulling simulations

Dist.	LH	PC1	PC2	PC3
	I1161-C1203	-0.16	-0.04	0.14
	K1177-N1241	0.36	0.45	0.66
	A1212-H1249	-0.33	0.10	-0.20
	Q1225-H1261	0.00	0.32	-0.04

Extended Data Fig. 4 | Correlation between distances of amino acid pairs and LH domain principal components. Correlation coefficients between the Cα-Cα distances of the three amino-acid pairs that were converted into cysteine pairs to generate LH+LH^{Cys}-NOMPC::GFP (Fig. 5 and Extended Data Fig. 5) and the principal components (PCs) of the LH domain in equilibrium (left), pushing (middle) and pulling (right) simulations. Correlation coefficients whose absolute values exceed 0.5 are highlighted in blue. The positions of the respective amino-acid pairs and their Cα-Cα distances in equilibrium (without forcing) and non-equilibrium (with pushing force) simulations are indicated in Fig. 5b.

https://doi.org/10.1038/s41593-024-01849-3

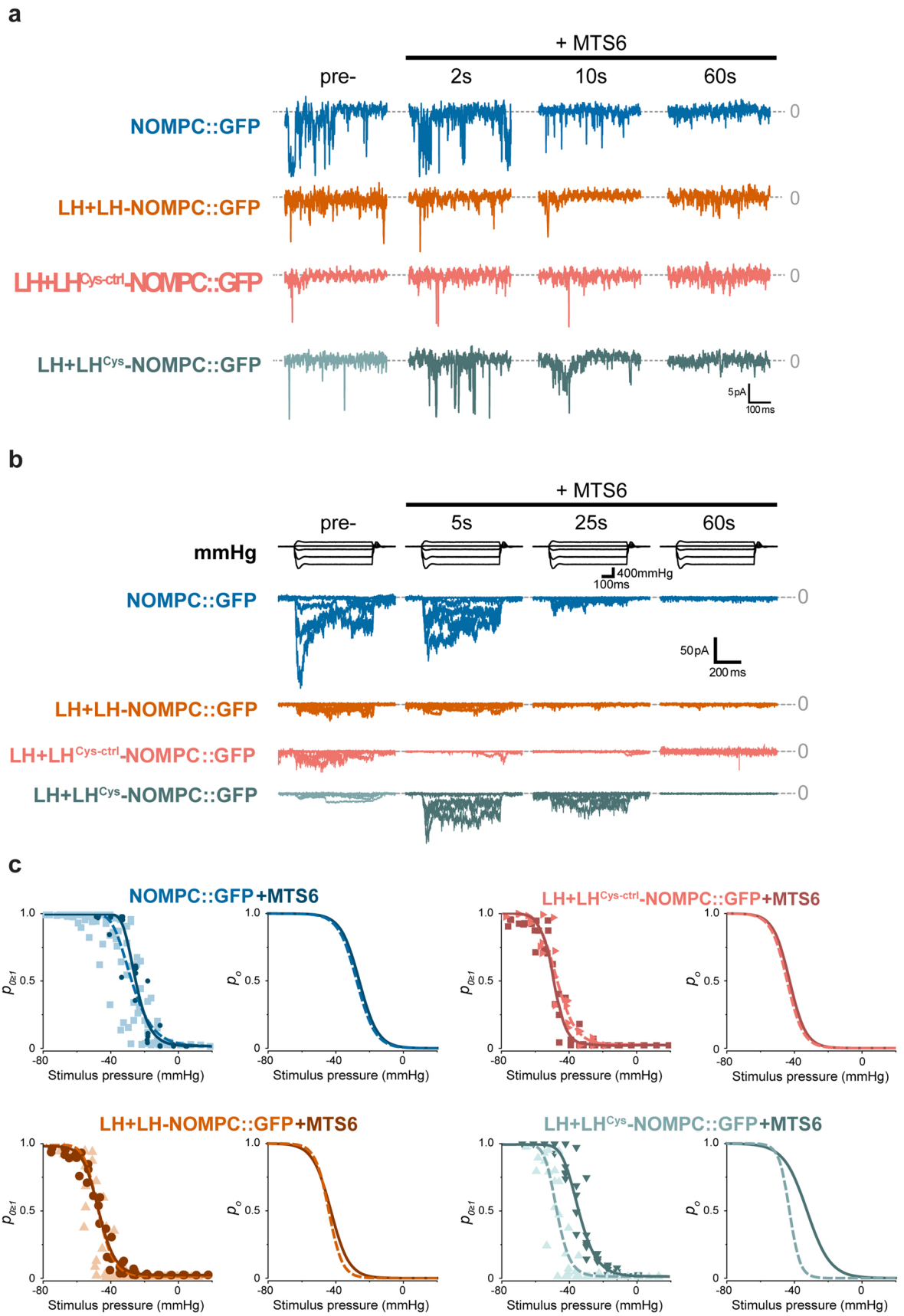

Extended Data Fig. 5 | See next page for caption.

https://doi.org/10.1038/s41593-024-01849-3

Extended Data Fig. 5 | Transient effects of crosslinking cysteine pairs on in vitro NOMPC function. a, Representative traces of spontaneous currents recorded before and at different times after application of the crosslinking agent MTS6. **b**, Corresponding traces of pressure-evoked currents. MTS6 transiently increases spontaneous and pressure-evoked currents of LH+LH^{Cys}-NOMPC::GFP carrying three cysteine pairs (I1161C–C1203, K1177C–N1241C, A1212C–H1249C), but not of NOMPC::GFP, LH-LH-NOMPC::GFP, and also LH+LH$^{Cys\text{-}ctrl}$-NOMPC::GFP, in which two of the three cysteine pairs of LH+LHCys-NOMPC::GFP (K1177C–N1241C and A1212C–H1249C) are reverted back to single cysteines (K1177C and A1212C). **c**, Corresponding pressure(P)-dependent open probability p_o (P) before (hatched lines) and immediately after (solid lines) MTS6 application (N = 5 cells per construct). For each construct, $p_{o,\geq 1}$ (P) = 1 − (1 − p_o (P))^N (left) and p_o (P) (right) are shown. MTS6 shifts p_o (P) to lower pressure amplitudes for LH+LH^{Cys}-NOMPC::GFP, but not NOMPC::GFP, LH + LH-NOMPC::GFP, and LH+LH$^{Cys\text{-}ctrl}$-NOMPC::GFP. This narrows down the effect to modification of the two cysteine pairs that are present only in LH+LH^{Cys}-NOMPC::GFP (K1177C–N1241C and A1212C–H1249C) and that, according to our molecular dynamics (MD) simulations, change distance in response to force (Fig. 5b). At the same time, it shows that this increase arises neither from modification of the cysteine pair that is present in both constructs (I1161C–C1203, which does not change distance in our MD simulations (Fig. 5b)), nor from modification of the two single cysteines K1177C and A1212C. In principle, the effect could arise from modification of the two single cysteines N1241C and H1249C, yet this possibility seems unlikely, not only because MTS6 crosslinks cysteine pairs, but because MTS6 does not randomly impair LH+LH^{Cys}-NOMPC::GFP, but shifts its p_o (*P*) to that of NOMPC::GFP.

nature portfolio

Corresponding author(s): Martin Göpfert

Last updated by author(s): 2024-08.16

Reporting Summary

Nature Portfolio wishes to improve the reproducibility of the work that we publish. This form provides structure for consistency and transparency in reporting. For further information on Nature Portfolio policies, see our Editorial Policies and the Editorial Policy Checklist.

Statistics

For all statistical analyses, confirm that the following items are present in the figure legend, table legend, main text, or Methods section.

n/a	Confirmed	
☐	☒	The exact sample size (*n*) for each experimental group/condition, given as a discrete number and unit of measurement
☐	☒	A statement on whether measurements were taken from distinct samples or whether the same sample was measured repeatedly
☐	☒	The statistical test(s) used AND whether they are one- or two-sided *Only common tests should be described solely by name; describe more complex techniques in the Methods section.*
☐	☒	A description of all covariates tested
☐	☒	A description of any assumptions or corrections, such as tests of normality and adjustment for multiple comparisons
☐	☒	A full description of the statistical parameters including central tendency (e.g. means) or other basic estimates (e.g. regression coefficient) AND variation (e.g. standard deviation) or associated estimates of uncertainty (e.g. confidence intervals)
☐	☒	For null hypothesis testing, the test statistic (e.g. *F*, *t*, *r*) with confidence intervals, effect sizes, degrees of freedom and *P* value noted *Give P values as exact values whenever suitable.*
☒	☐	For Bayesian analysis, information on the choice of priors and Markov chain Monte Carlo settings
☒	☐	For hierarchical and complex designs, identification of the appropriate level for tests and full reporting of outcomes
☒	☐	Estimates of effect sizes (e.g. Cohen's *d*, Pearson's *r*), indicating how they were calculated

Our web collection on statistics for biologists contains articles on many of the points above.

Software and code

Policy information about availability of computer code

Data collection	Spike2(v10.05), Polytec Acquisition software(v9.4), Patchmaster software (HEKA, version v2x90.2), Leica X software
Data analysis	OriginPro2020(v9.7.0.188), Excel(v2308), Spike2(v10.05), Polytec Acquisition software(v9.4), ImageJ(v1.53t; Java1.8), Patchmaster software (HEKA, v2x90.2),Clampfit (Molecular Devices), CHARMM-GUI, GROMACS2019, DynDom, PyMol(v2.5.2), NetworkView

For manuscripts utilizing custom algorithms or software that are central to the research but not yet described in published literature, software must be made available to editors and reviewers. We strongly encourage code deposition in a community repository (e.g. GitHub). See the Nature Portfolio guidelines for submitting code & software for further information.

Data

Policy information about availability of data

All manuscripts must include a data availability statement. This statement should provide the following information, where applicable:

- Accession codes, unique identifiers, or web links for publicly available datasets
- A description of any restrictions on data availability
- For clinical datasets or third party data, please ensure that the statement adheres to our policy

All data and materials to draw the conclusions of this manuscript are presented in the main text and figures, and the extended data figures and movies.

Original data linked to this publication can be found at https://doi.org/10.25625/LVUTCE. The NOMPC.L structure used for the molecular dynamic simulations is accessible at protein data bank (pdb) (rcsb.org/structure/5VKQ).

Research involving human participants, their data, or biological material

Policy information about studies with human participants or human data. See also policy information about sex, gender (identity/presentation), and sexual orientation and race, ethnicity and racism.

Reporting on sex and gender	N/A
Reporting on race, ethnicity, or other socially relevant groupings	N/A
Population characteristics	N/A
Recruitment	N/A
Ethics oversight	N/A

Note that full information on the approval of the study protocol must also be provided in the manuscript.

Field-specific reporting

Please select the one below that is the best fit for your research. If you are not sure, read the appropriate sections before making your selection.

☒ Life sciences ☐ Behavioural & social sciences ☐ Ecological, evolutionary & environmental sciences

For a reference copy of the document with all sections, see nature.com/documents/nr-reporting-summary-flat.pdf

Life sciences study design

All studies must disclose on these points even when the disclosure is negative.

Sample size	No statistical methods were used to pre-determine sample sizes but our sample sizes are similar to those reported in previous publications (Refs. 18,31,34,42,48).
Data exclusions	No data were excluded from the analyses, except for patch recordings when experiments were incomplete because the patch had ruptured during the experiments.
Replication	Patch-clamp data derives from independently measured out-side-out patches. Electrophysiology and gating compliance data derives from the same, independently measured animals.
Randomization	Experiments were randomized with respect to genotypes and stimulation amplitudes.
Blinding	Investigators were blinded initially for genotypes during experiment and outcome assessment, yet blinding was given up in the course of the study because it turned out to be in-effective as genotypes could be inferred easily from phenotypes.

Reporting for specific materials, systems and methods

We require information from authors about some types of materials, experimental systems and methods used in many studies. Here, indicate whether each material, system or method listed is relevant to your study. If you are not sure if a list item applies to your research, read the appropriate section before selecting a response.

Materials & experimental systems

n/a	Involved in the study
☐	☒ Antibodies
☐	☒ Eukaryotic cell lines
☒	☐ Palaeontology and archaeology
☐	☒ Animals and other organisms
☒	☐ Clinical data
☒	☐ Dual use research of concern
☒	☐ Plants

Methods

n/a	Involved in the study
☒	☐ ChIP-seq
☒	☐ Flow cytometry
☒	☐ MRI-based neuroimaging

Antibodies

Antibodies used	FluoTag®-X4 Atto 488nm anti-GFP (1:1000, NanoTag Biotechnologies, N0304) Cy3-conjugated goat anti-HRP (1:300, Jackson ImmunoResearch, 123-165-021) rabbit anti-NOMPC-EC (kindly provided by Yuh-Nung Jan, 1:500) Alexa Fluor 488 goat anti-rabbit (Thermo Fisher Scientific, A-11008, 1:1000)
Validation	anti-NOMPC-EC (Zhang et al., 2015), anti-HRP (Katana et al. 2019), anti-GFP confirmed with in vivo localization of NOMPC in S2 cells and at the tip of the cilium (see Extended Data Figs. 1a and 2).

Eukaryotic cell lines

Policy information about cell lines and Sex and Gender in Research

Cell line source(s)	Schneider's Drosophila Line 2 [D. Mel. (2), SL2] (ATTC CRL-1963)
Authentication	Proof of cell line authentication was provided by the vendor (ATCC, CRL-1963). In addition, we examined the morphology of the cells and observed the successful expression of the fusion proteins with the Gal4/UAS-System (Act5c>Gal4 plasmid and UAST-attP-constructs)
Mycoplasma contamination	Mycoplasma contamination is routinely checked every 4 months (MycoSPY® Master Mix, Biontex). PCR tests were negative throughout.
Commonly misidentified lines (See ICLAC register)	No commonly misidentified cell lines were used in the study.

Animals and other research organisms

Policy information about studies involving animals; ARRIVE guidelines recommended for reporting animal research, and Sex and Gender in Research

Laboratory animals	Drosophila melanogaster, adults (2-5 after eclosure)
Wild animals	No wild animals were used in this study.
Reporting on sex	Flies of either sex were used as neither Johnston's organ function nor auditory mechanics seem to be sex-specific.
Field-collected samples	No field-collected samples were used in this study.
Ethics oversight	Dealing with an invertebrate species, no ethical approval was needed. Experiments were carried out in accordance with German Federal Regulations (license Gen.Az 501.40611/0166/501).

Note that full information on the approval of the study protocol must also be provided in the manuscript.